

AD _____

Award Number: DAMD17-99-1-9121

TITLE: Improved MR Images of Breast Lesions with Fast
Spectroscopic Imaging

PRINCIPAL INVESTIGATOR: Gregory S. Karczmar, Ph.D.

CONTRACTING ORGANIZATION: The University of Chicago
Chicago, Illinois 60637

REPORT DATE: October 2002

TYPE OF REPORT: Annual

PREPARED FOR: U.S. Army Medical Research and Materiel Command
Fort Detrick, Maryland 21702-5012

DISTRIBUTION STATEMENT: Approved for Public Release;
Distribution Unlimited

The views, opinions and/or findings contained in this report are those of the author(s) and should not be construed as an official Department of the Army position, policy or decision unless so designated by other documentation.

20030529 174

REPORT DOCUMENTATION PAGE

Form Approved
OMB No. 074-0188

Public reporting burden for this collection of information is estimated to average 1 hour per response, including the time for reviewing instructions, searching existing data sources, gathering and maintaining the data needed, and completing and reviewing this collection of information. Send comments regarding this burden estimate or any other aspect of this collection of information, including suggestions for reducing this burden to Washington Headquarters Services, Directorate for Information Operations and Reports, 1215 Jefferson Davis Highway, Suite 1204, Arlington, VA 22202-4302, and to the Office of Management and Budget, Paperwork Reduction Project (0704-0188), Washington, DC 20503

1. AGENCY USE ONLY (Leave blank)		2. REPORT DATE October 2002	3. REPORT TYPE AND DATES COVERED Annual (15 Sep 01 - 14 Sep 02)	
4. TITLE AND SUBTITLE Improved MR Images of Breast Lesions with Fast Spectroscopic Imaging			5. FUNDING NUMBERS DAMD17-99-1-9121	
6. AUTHOR(S) : Gregory S. Karczmar, Ph.D.				
7. PERFORMING ORGANIZATION NAME(S) AND ADDRESS(ES) The University of Chicago Chicago, Illinois 60637 E-Mail: gskarczm@midway.uchicago.edu			8. PERFORMING ORGANIZATION REPORT NUMBER	
9. SPONSORING / MONITORING AGENCY NAME(S) AND ADDRESS(ES) U.S. Army Medical Research and Materiel Command Fort Detrick, Maryland 21702-5012			10. SPONSORING / MONITORING AGENCY REPORT NUMBER	
11. SUPPLEMENTARY NOTES				
12a. DISTRIBUTION / AVAILABILITY STATEMENT Approved for Public Release; Distribution Unlimited			12b. DISTRIBUTION CODE	
13. ABSTRACT (Maximum 200 Words) The goal of this research is to use high spectral and spatial resolution (HiSS) MR imaging to improve images of human breast. Our work on the application of HiSS to improve anatomic and functional imaging was first described in a paper in Academic Radiology. Related work from this laboratory is presented in a number of other publications. Work from other laboratories shows that closely related methods also provide advantages for anatomic and functional MRI. Our funding from the Army has supported implementation of HiSS on clinical scanners and preliminary tests of the method in women with normal breasts and women with breast lesions. The results demonstrate that HiSS provides improved fat-suppression, contrast and edge delineation compared to conventional imaging. The funded work resulted in several publications listed in this report. We are continuing to optimize this method and are applying for additional funding so that it can be tested in a larger group of women.				
14. SUBJECT TERMS: breast cancer, magnetic resonance imaging			15. NUMBER OF PAGES 50	
			16. PRICE CODE	
17. SECURITY CLASSIFICATION OF REPORT Unclassified	18. SECURITY CLASSIFICATION OF THIS PAGE Unclassified	19. SECURITY CLASSIFICATION OF ABSTRACT Unclassified	20. LIMITATION OF ABSTRACT Unlimited	

NSN 7540-01-280-5500

Standard Form 298 (Rev. 2-89)
Prescribed by ANSI Std. Z39-18
298-102

Table of Contents

Cover.....	1
SF 298.....	2
Table of Contents.....	3
Introduction.....	4
Body.....	5
Key Research Accomplishments.....	5
Reportable Outcomes.....	5
Conclusions.....	7
References.....	7
Appendices.....	8

- (2) **INTRODUCTION:** Narrative that briefly (one paragraph) describes the subject, purpose, and scope of the research.

The goal of this research is to use high spectral and spatial resolution (HiSS) MR imaging to improve images of human breast. Our work on the application of HiSS to improve anatomic and functional imaging was first described in a paper in Academic Radiology [1]. Related work from this laboratory is presented in a number of other publications [2-9]. Work from other laboratories shows that closely related methods also provide advantages for anatomic [10] and functional [11-14] MRI.

This significant body of work provides support for the feasibility of ongoing experiments in this laboratory. Specifically, we expect to 1) improve separation of water and fat signals 2) increase image contrast 3) increase sensitivity to contrast agents and to local physiology – and as a result improve detection of suspicious lesions such as cancers and particularly delineation of tumor edges. We expect that this will increase the sensitivity and specificity of MR scans for breast cancer. To achieve these goals our original 'statement of work' was as follows:

A. Implementation of FSI methods on a clinical Scanner: Our clinical whole body scanners will be programmed to produce oscillating gradients during the decay of the proton FID so that a series of gradient echoes can be detected following excitation.

B. Processing FSI Data: Spectral information in FSI data sets will be analyzed to reduce the effects of resonance offset in MR images. Then the corrected FSI data will be used to synthesize images in which intensity is proportional to the peak intensity, linewidth, integral, and resonance frequency of resonances.

C. A phantom which contains large magnetic susceptibility gradients and both lipid and water compartments will be constructed to allow evaluation and optimization of FSI methods. Conventional spectroscopic images which use only phase encoding gradients to obtain spatial information will provide 'gold standard' images of the phantom.

D. Studies of patients: Women who are at increased risk for breast cancer and attend our 'high risk' clinic, and patients who are treated with neoadjuvant therapy for breast cancer will be recruited for MR studies:

1. **Approximately 25 patients per year will be studied using fast spectroscopic imaging without contrast agents.** FSI will be correlated quantitatively with conventional MRI and biopsy.

2. **Approximately 25 patients per year will be given contrast.** Time resolved FSI images of contrast uptake will be analyzed to measure rates of contrast uptake and accurately identify the boundaries of enhancing regions. T_1 -weighted and T_2^* -weighted images of contrast agent uptake will be synthesized. FSI images will be correlated quantitatively with conventional MRI and biopsy

3. **Quantitative analysis of FSI data and quantitative comparison with conventional images:** We will extend previous work of Drs. Guilhuijs and Giger to provide quantitative analysis of FSI and conventional images. We will compare edge sharpness, texture, temporal and spatial gradients in contrast media uptake, signal-to-noise ratio, and contrast-to-noise ratio in FSI and conventional MR images.

E. MR data will be correlated with biopsy, conventional MR images, and mammography.

(3) **BODY:**

During the 2nd budget year we made significant progress towards achieving the specific aims of the proposal. We have worked towards completion of all of the components of the statement of work listed above:

SOWA: Upgraded our FSI pulse sequence so that we can perform fast echo planar spectroscopic imaging on the new GE scanners that were recently installed at the University of Chicago. The new sequence (referred to as the following as high resolution spectroscopic imaging – or HiSS) is integrated into the standard clinical breast exam so that it is more efficient to study a larger number of patients.

SOWB. We continued development of methods for processing the data and quantitative comparison of HiSS datasets with conventional MRI.

At the same time – we continued limited studies of rodents to help us to optimize data collection and processing. In particular, we have acquired high spectral and spatial resolution images of rat brain – because the well defined anatomy allows us to evaluate the data acquisition and processing. As before, the costs of the rat experiments are not supported by this grant, but the work contributes to our implementation of HiSS.

SOWD. We have increased the number of patients and volunteers studies. Specifically we imaged normal volunteers (n=15) and women with biopsy-confirmed breast cancer (n=7) and women with suspicious lesions on mammography (n=5). We demonstrated quantitatively that fat-suppression, edge delineation, and image texture were improved in images derived from HiSS data compared to conventional images. HiSS data acquired pre- and post- contrast media injection showed features not evident in conventional images.

The work is described in detail in the manuscripts that are included.

(4) **KEY RESEARCH ACCOMPLISHMENTS:** Bulleted list of **key** research accomplishments emanating from this research

- Upgrades of fast HiSS MR imaging methods on new clinical scanners. The HiSS pulse sequences can not be integrated into standard clinical scans
- HiSS scans of breast of healthy volunteers, women with suspicious breast lesions, and women who are being treated for breast cancer.
- Quantitative analysis of HiSS and conventional image texture and edge delineation – demonstrating that HiSS increases these measures of image quality.

(5) **REPORTABLE OUTCOMES::**

– manuscripts, abstracts, presentations;

- A paper describing aspects of this work has been accepted for publication in Radiology. We attach the manuscript. This is an important step forward for this work since it will describe this technology to Radiology's very large audience of practicing academic Radiologists and hopefully encourage them to evaluate it in their own institutions.

- An invited paper in Academic Radiology (in press) further demonstrates advantages of HiSS MRI of breast compared to conventional MRI.

- We are in the process of writing a second paper that analyzes the requirement for high spectral resolution, and compares high spectral and spatial resolution images to those obtained using the Dixon method – which uses only two points of spectral resolution.

- A third paper which reports related research on the inhomogeneous broadening of water resonances in tumors in press in NMR in Biomedicine.

- We presented the work at last year's ISMRM and are submitting two abstracts to this year's ISMRM (International Society of Magnetic Resonance in Medicine). I was also invited to present the work at the Contrast Media Research Association meeting this summer.

List of papers in press or in preparation:

1. Karczmar GS, Du W, Bick U, MacEneany P, Du Y, Fan X, Zamora M, Lipton M; Spectrally inhomogeneous effects of contrast agents in breast lesions detected by high spectral and spatial resolution MRI; Academic Radiology, in press

2. Du W, Du Y, Bick U, Fan X, MacEneany P, Zamora M, Medved M, Karczmar GS; High spectral and spatial resolution MR imaging of breast – preliminary experience. Radiology, in press.

3. Medved M, Du W, Du Y, Bick U, Fan X, MacEneany P, Zamora M, Karczmar G; Effect of increased spectral resolution on water-fat separation in breast MR imaging. Manuscript in preparation for Journal of Magnetic Resonance Imaging

– degrees obtained that are supported by this award;

Al-Hallaq- Ph.D . awarded July, 2000

Weiliang Du, PhD. Expected 2002

– funding applied for based on work supported by this award;

1. We have applied for a DOD 'Clinical Bridge Award' to continue and expand the work supported by the present grant.

2. We sent a proposal to the Army's prostate cancer research program to extend the present work to improve imaging of the prostate. This proposal was recently recommended for funding by the Army DAMD17-02-1-0033.

3. We submitted a proposal to NIH to further develop high spectral and spatial resolution MRI based on studies of rodent tumor models. This proposal received a good priority score (160) and it appears likely that funding will be awarded.

4. This work was a critical component of an instrumentation proposal to NIH that requested funding for a whole body scanner. The scanner would greatly enhance our

clinical research capability and allow us to scan a much larger number of women with breast lesions and greatly reduced cost.

CONCLUSIONS: Our results to date demonstrate quantitatively that there are significant advantages associated with high spectral and spatial resolution imaging. These include

1. Greatly improved suppression of fat signals in breast
2. Improved delineation of edges, for example tumor boundaries
3. Greatly increased sensitivity to contrast agents.
4. Potential for sensitivity to subvoxelar environments – perhaps microscopic environments represented by the various components of inhomogeneously broadened water resonances.

During the coming year we hope to expand the number of patients and volunteers we scan and further improve our methods for data analysis. We anticipate that the no. of patients scanned by the end of the funding period will be sufficient to allow more definitive comparison of HiSS and conventional MRI and perhaps a preliminary estimate of the sensitivity and specificity of HiSS MRI for malignancies.

REFERENCES:

1. Kovar, D. A.; Al-Hallaq, H. A.; Zamora, M. A.; River, J. N.; Karczmar, G. S. Fast spectroscopic imaging of water and fat resonances to improve the quality of MR images. *Acad Radiol* 5(4):269-275; 1998.
2. Kuperman, V.; River, J. N.; Karczmar, G. S. High Resolution Spectroscopic Images of Tumors. *International Society for Magnetic Resonance in Medicine* ; 1995.
3. Al-Hallaq, H. A.; Zamora, M.; Fish, B. L.; Farrell, A.; Moulder, J. E.; Karczmar, G. S. MRI measurements correctly predict the relative effect of tumor oxygenating agents on hypoxic fraction in rodent BA1112 tumors. *Int J Radiat Oncol Biol Phys* in press; 2000.
4. Al-Hallaq, H. A.; Karczmar, G. High resolution ¹H spectroscopic imaging of the water and fat resonances in human breast. *International Society for Magnetic Resonance in Medicine* 2; 1997.
5. Al-Hallaq, H. A.; River, J. N.; Zamora, M.; Oikawa, H.; Karczmar, G. S. Correlation of magnetic resonance and oxygen microelectrode measurements of carbogen-induced changes in tumor oxygenation. *Int J Radiat Oncol Biol Phys* 41(1):151-159; 1998.
6. Karczmar, G. S.; Fan1, X.; Al-Hallaq1, H. A.; Zamora, M.; River, J. N.; Rinker-Schaeffer, C.; Zaucha, M.; Tarlo, K.; Kellar, K. Uptake of a Superparamagnetic Contrast Agent Imaged by MR with High Spectral and Spatial Resolution. *Magnetic Resonance in Medicine* 43:633-639; 2000.
7. Fan, X.; River, J. N.; Zamora, M.; Tarlo, K.; Kellar, K.; Rinker-Schaeffer, C.; Karczmar, G. S. Differentiation of Non-Metastatic and Metastatic Rodent Prostate Tumors with High Spectral and Spatial Resolution MRI. *Magnetic Resonance in Medicine* in press; 2001.
8. Karczmar, G.; X Fan1, H. A.-H.; River, J.; Tarlo, K.; Kellar, K.; Zamora, M.; Rinker-Schaeffer, C.; Lipton, M. J. Functional and Anatomic Imaging of Tumor Vasculature: High Resolution MR Spectroscopic Imaging Combined with a Superparamagnetic Contrast Agent. *Academic Radiology* in press; 2001.

9. Oikawa, H.; Al-Hallaq, H. A.; Lewis, M. Z.; River, J. N.; Kovar, D. A.; Karczmar, G. S. Spectroscopic imaging of the water resonance with short repetition time to study tumor response to hyperoxia. *Magn Reson Med* 38(1):27-32; 1997.
10. Sarkar, S.; Heberlein, K.; Metzger, G. J.; Zhang, X.; Hu, X. Applications of high-resolution echoplanar spectroscopic imaging for structural imaging. *J Magn Reson Imaging* 10(1):1-7; 1999.
11. Zhong, J.; Kennan, R.; Schaub, M.; Gore, J. C. Measurements of transient contrast enhancement by localized water NMR spectroscopy. *J Magn Reson B* 104(2):111-118; 1994.
12. Zhong, K.; Li, X.; Shachar-Hill, Y.; Picart, F.; Wishnia, A.; Springer, C. S. Magnetic susceptibility shift selected imaging (MESSI) and localized (1)H(2)O spectroscopy in living plant tissues. *NMR Biomed* 13(7):392-397; 2000.
13. Posse, S.; Wiese, S.; Gembris, D.; Mathiak, K.; Kessler, C.; Grosse-Ruyken, M. L.; Elghahwagi, B.; Richards, T.; Dager, S. R.; Kiselev, V. G. Enhancement of BOLD-contrast sensitivity by single-shot multi-echo functional MR imaging [In Process Citation]. *Magn Reson Med* 42(1):87-97; 1999.
14. Posse, S.; Dager, S. Using Functional Proton Spectroscopic Imaging. *International Society for Magnetic Resonance in Medicine* ; 1995.

APPENDIX

1. Karczmar GS, Du W, Bick U, MacEneany P, Du Y, Fan X, Zamora M, Lipton M; Spectrally inhomogeneous effects of contrast agents in breast lesions detected by high spectral and spatial resolution MRI; *Academic Radiology*, in press
2. Medved M, Du W, Du Y, Bick U, Fan X, MacEneany P, Zamora M, Karczmar G; High spectral and spatial resolution MRI aids water-fat separation in MRI of the breast. Abstract submitted to the International Society of Magn. Reson. In Med, 2002 meeting.
3. Fan X, Du W, MacEneany P, Zamora M, Karczmar G; Using high spectral and spatial resolution MRI to detect inhomogeneous broadening of the water resonance in rat brain; Abstract submitted to the International Society of Magn. Reson. In Med, 2002 meeting.

The effect of varying spectral resolution on the quality of HiSS MR images of the breast

Running title: Spectral resolution in MR of breast

M. Medved¹, PhD, W. Du¹, MS, M. A. Zamora¹, BA, X. Fan¹, PhD
O. I. Olopade², MD, P. M. MacEneaney¹, MD, G. Newstead¹, MD,
G. S. Karczmar¹, PhD

¹Department of Radiology and
²Section of Hematology and Oncology,
The University of Chicago,
5841 S. Maryland Ave
Chicago, Illinois 60637

Corresponding author:

Milica Medved

The University of Chicago
Department of Radiology, MC 2026
5841 S. Maryland Ave
Chicago, Illinois 60637

Phone: 773-702-4711

Fax: 773-834-3193

Email: mmedved@uchicago.edu

This work was supported by grants from the NCI (RO1CA75476 & RO1CA78803), the
Army Breast Cancer Research Program (DAMD 17-99-1-9121) and General Electric
Medical Systems.

This work was presented at ISMRM meeting 2002.

SUBMITTED TO JMRI

Abstract:

Purpose: To evaluate the effect of varying spectral resolution on image quality of high spectral and spatial resolution (HiSS) imaging.

Materials and Methods: Five women with suspicious breast lesions and six healthy volunteers were scanned using echo-planar spectroscopic imaging at 1.5 Tesla with 0.75 - 1 mm in-plane resolution, and 2.6 Hz spectral resolution. Time domain data were truncated to obtain proton spectra in each voxel with varying (2.6 - 83.3 Hz) resolution. Images with intensity proportional to water and fat signal peak heights were synthesized. Changes in water signal lineshape following contrast injection were analyzed.

Results: Fat suppression is optimized at ~10 Hz spectral resolution, and is significantly improved by removal of wings of the fat resonance using a Lorentzian fit. Water resonance is often inhomogeneously broadened, and very high spectral resolution is necessary to resolve individual components. High spectral resolution is required for optimal delineation of anatomic features with very high T_2^* (e.g. within a lesion), and for detection of often subtle effects of contrast agents on water signal lineshape.

Conclusion: Despite a trade-off between the spectral resolution and signal-to-noise ratio, it is beneficial to acquire data at the highest spectral resolution currently attainable at 1.5 Tesla.

Key Words: high spectral and spatial resolution spectroscopic imaging; echo-planar spectroscopic imaging; contrast agent effects; fat suppression; breast; cancer.

Introduction

The quality of MR images of breast has been enhanced by a number of technical improvements including improved fat saturation [1, 2], low spectral resolution spectroscopic imaging [3-11] for improved fat and water separation, and quantitative and semi-quantitative analysis of contrast media uptake kinetics [12-17]. Despite these advances, the high sensitivity of MRI combined with limited specificity still leads to a large number of false positives [18-25]. This is unacceptable if MRI is to be used in a large population of women – e.g. women who are at high risk for breast cancer.

High spectral and spatial resolution (HiSS) MRI increases the information content of MR data, and as a result, has the potential to increase sensitivity and specificity. HiSS data have spatial resolution similar to that of conventional MRI or higher and, in addition, a high resolution spectrum of the water and fat resonances is associated with each image voxel. Work in this laboratory demonstrated advantages of HiSS MRI of the breast [26]. Other work suggests that HiSS MRI in various forms – including multiple gradient echo imaging [27] – is advantageous for functional and anatomic MRI [26-33]. The advantages include improved fat suppression or fat/water separation, increased anatomic detail and strong $T2^*$ contrast with lessened artifacts due to intravoxel dephasing effects. In addition, HiSS provides increased sensitivity to effects of contrast agents. While conventional MRI detects only changes in $T1$ and/or $T2^*$, HiSS can detect subtle changes in water resonance line shape following contrast media injection that may indicate sub-voxelar regions of high vascular density. [26, 29, 34] Studies of rodent prostate cancer suggested that HiSS MRI differentiates between metastatic and non-metastatic cancers

based on the texture, edges, and contrast media uptake characteristics in the primary tumor [34]. However, high spectral resolution comes with a cost: it entails loss of signal-to-noise ratio and increased image acquisition time. The purpose of the present work is to evaluate the effects of increasing spectral resolution on various anatomic and functional parameters in HiSS images. This is accomplished by processing HiSS data sets at spectral resolutions ranging from 83.3 Hz to 2.6 Hz.

Methods

Patient recruitment

Six women without evidence of breast abnormalities and 5 women with mammographically suspicious breast lesions were scanned. The patients were recruited from the University Cancer Risk Clinic and the mammography service. The reference (healthy) volunteers were recruited from the clinic staff. All patients were studied under a protocol approved by the University Institutional Review Board after informed consent was obtained.

Image acquisition

MR images were acquired on 1.5 Tesla GE SIGNA scanners equipped with ECHO SPEED™ GRADIENTS (GE Medical Systems, Waukesha Wisconsin). The body coil was used for excitation and a phased array coil designed for breast imaging was used to detect signal. HiSS images were acquired using echo-planar spectroscopic imaging (EPSI). [35-37] The EPSI pulse sequence was composed of a slice-selective excitation pulse (4 mm slice thickness), a phase encoding gradient with 256 phase encoding steps and a train of 128 gradient echoes with 256 or 384 sampled points per gradient echo.

This produced images with 256 or 384 x 256 points of spatial resolution, with resulting in-plane resolution of 750 - 1000 microns, and 128 bins of spectral resolution. The gradient echo train was sampled at a bandwidth of 62.5 kHz, so that the FID was sampled for approximately 400 ms. As a result, maximum spectral resolution was 2.6 Hz, or 0.041ppm. The acquisition time per slice under these conditions was approximately 130 seconds. The fat and water peaks were separated by more than 64 spectral bins, so that N/2 ghost peaks would not overlap fat or water signal. These ghost peaks are a consequence of the uneven sampling of the FID, analogous to the N/2 ghosting inherent to EPI sequences. Typically, only a single slice was imaged in each patient. The patients were imaged both pre- and post- contrast agent injection (0.1 mM per kg of patient weight, OmniscanTM, Nycomed Amersham), while the healthy volunteers did not receive contrast agent.

Image processing

The EPSI data were processed with a 3D Fourier transform to obtain a high-resolution proton spectrum in every voxel of the imaged slice. An algorithm was used on the resulting data to detect the fat and water peak frequencies, in the following manner:

1. The highest peak in each voxel was identified, and a map of its frequency was generated.
2. The voxel of highest peak height intensity was *a priori* identified by the software as either fat or water, and fat and water frequencies were determined for this voxel. Alternatively, one or more seed voxels were chosen in which the fat and/or water peaks were manually identified.

3. The voxel to be processed next, V_N , was selected as the highest intensity voxel adjacent to the already processed voxels.
4. The frequency, f_{VN} , of the highest peak in V_N was compared to the expected fat frequency, f_{exp} , equal to the average of fat frequencies in neighboring, already processed voxels. Based on the separation of f_{VN} and f_{exp} , the highest peak in V_N was identified as either fat or water, and hence the fat frequency in V_N was determined.
5. The algorithm resumed at point 3, until all the voxels were processed, yielding a map of the fat frequency or, equivalently, the B_0 map.

In most cases, this algorithm did not require human intervention. It also effectively avoided errors due to Nyquist ghosting, inherent in EPI, and hence in EPSI. In our EPSI images, these show as spectral ghosts due to uneven sampling of the FID at high k_x values.

After the fat frequency map, and hence the water frequency map, was determined, water peak height and peak integral images were constructed, as well as the analogous fat images. The high-resolution spectrum in each voxel was fit using a Lorentzian approximation for the fat and water peaks, and for any N/2 spectral ghosts. The Lorentzian fits for fat peaks and N/2 ghost peaks were then subtracted to allow accurate analysis of the water signal. This was particularly important for detection of small amounts of water in the presence of large fat signals. As the water signal was often inhomogeneously broadened, the peak and integral water images were not obtained from the fit parameters. Rather, after subtraction of the fits for fat and N/2 ghosts, the

maximum of the isolated water signal in each voxel was used to construct water peak height images, and the integral in a 25 Hz range around the water peak frequency was used to construct integral images.

This procedure was repeated to construct water and fat peak height images at varying spectral resolutions (See Fig. 3). The spectral resolution was varied between 2.6 – 83.3 Hz by either using the full FID with all 128 echoes, or truncating the FID at $N = 64, 32, 16, 8$ or 4 echoes, and substituting the remaining echoes with zeros. This resulted in effective spectral resolutions of 2.6 Hz (at full resolution), 5.2 Hz, 10.4 Hz, 20.8 Hz, 41.6 Hz and 83.3 Hz. Truncation was preferred over exponential or other smoothing, as the purpose was to explore faster data acquisition with a reduced number of echoes, rather than image processing methods.

Image characterization

The quality of the water peak height images was quantified based on fat suppression and contrast. The effectiveness of fat/water separation is assessed by calculating a fat suppression ratio, FSR. We define FSR as the ratio of the average intensity of 'water peak height images' in the voxels containing predominantly water to the average signal in the voxels containing predominantly fat. [26] Thanks to high spatial resolution of our images, all but few voxels fall into one of these two categories. Since ideally, only the water signal contributes to these images, signal in voxels that contain predominantly fat should be minimized, and signal in voxels that contain predominantly water should be maximized. Therefore, effective water/fat separation should increase FSR.

The contrast within the water image was assessed via a 'texture' parameter, S_r , which describes the non-uniformity of the signal. S_r is defined as the increase in the surface area of measured signal, (when intensity is plotted against the 2D xy plane of imaged slice), relative to its projection, S_{xy} , onto this xy plane: [26, 34]

$$S_r = \frac{\sum \sqrt{1 + f_x^2 + f_y^2} - S_{xy}}{S_{xy}} \quad (1)$$

If image intensity in the region of interest is constant, S_r is 0, and highly variable image intensity results in a large S_r . Only the voxels within the breast are included in calculations of FSR and S_r .

Contrast agent effects

To examine the effect of contrast agent, the post-contrast images were corrected for any motion that might have occurred between the pre-and post contrast acquisitions. Ten anatomical points of reference were selected, and a least-squares fit was performed for parameters of a linear transformation between the reference point coordinates in the two images. This procedure involved some smoothing between voxels, but dramatically improved the overlap of the pre- and post-contrast images. After the motion correction, the pre- and post contrast water peaks were corrected for global B_0 shifts caused by the contrast agent.

The difference of the post- and pre-contrast water resonance was calculated in each voxel. Voxels with inhomogeneously broadened water resonances were identified as the ones in which the difference spectra (spectrum post-contrast minus spectrum pre-

contrast) showed a strong peak whose width at the base was less than the average width of the pre- and post-contrast peaks. [38] In many cases, the width at the base could not be determined, and was approximated as twice the width at half-height. Only pixels in which the pre- and post-contrast resonances were above the 99% percentile noise level, and for which the difference peak was above $1.41 \times$ this value, were included.

Results

Figure 1a shows the dependence of FSR in water peak height images on number N of processed echoes in the acquired echo train, for five patients with breast lesions. The frequency resolution increases with N , as explained in the 'Image Processing' section. The values shown in diamonds were determined by fitting the fat peak with a Lorentzian function and subtracting this Lorentzian fit from the proton spectrum (see Fig. 2), to obtain an optimal value for water peak height in each voxel. The values shown in crosses were obtained from the peak height of the water resonance without subtracting the Lorentzian fit of the fat resonance. For all patients, the FSR increases sharply between $N = 4$ and $N = 32$. The FSR levels off at $N=32$ (10.4 Hz resolution) for all but one patient, whose FSR peaks at $N = 16$. At values of N higher than 32, there is a slight decrease in FSR, probably due to the decrease in signal-to-noise ratio. Subtracting the Lorentzian approximation to the fat peak from the proton spectrum significantly improves the FSR.

The advantages of peak fitting are greatest in the case where a small water resonance overlaps the wings of a very strong fat resonance. In Fig. 2, this effect is even more significant as, due to the spectral wraparound, the water resonance appears at 5.2 ppm,

very close to the fat peak. (The true frequency of the water resonance is arbitrarily set to 0ppm.) The removal of the fat signal by peak fitting allows a much more accurate measurement of the amplitude of the small water signal. Off-resonance fat components are also evident at ~ 4 ppm.

In Fig. 1b, we plot the dependence of S_r on N for the five patients with breast lesions. Similar to Fig. 1a, we show values obtained with (diamonds), and without (crosses) subtraction of the Lorentzian fit to the fat resonance. Fitting the fat peak improves S_r slightly, but not as significantly as it does the FSR. In all cases, S_r increases dramatically with increased frequency resolution, and levels off at $N = 64$ (5.2 Hz resolution). However, the calculations of S_r performed on the whole breast may obscure improvements in the texture in smaller but critical regions with long T_2^* , e.g. within the lesion. When S_r was calculated over smaller areas within the breast lesion, there were often improvements beyond $N = 64$, increasing by as much as 29% between $N = 64$ and $N = 128$.

Figure 3 shows the water and fat peak height images for a patient with infiltrating ductal carcinoma, calculated at three different spectral resolutions: 2.6 Hz ($N = 128$), 10.4 Hz ($N = 32$) and, 41.6 Hz ($N = 8$). At $N = 128$, inhomogeneities in the lesion are clearly visible, due to strong T_2^* contrast in regions where T_2^* is long. This contrast is reduced with reduced spectral resolution, which is particularly apparent at $N = 8$, where the lesion appears uniform.

Figure 4 shows spectra from five different voxels from one patient with infiltrating DCIS and one healthy volunteer at full, $N = 128$ (a) and two lower, $N = 64$ (b) and 32 (c) spectral resolutions. With reduced spectral resolution (b), the signal-to-noise ratio (S/N) is significantly improved, as would be expected due to elimination of low S/N points at the end of the FID. However, details of the water resonance are obscured. For example, at $N = 8$ (41.6 Hz spectral resolution) the water resonance is significantly broadened, and truncation artefacts are present. Even at $N = 32$ (10.4 Hz spectral resolution), the small shoulders on the water resonance (arrows) are not resolved. This may become an important consideration in contrast enhanced MRI (see below). In pixel #2, the water resonance is clearly resolved only at the highest spectral resolution.

In Figure 5, the pre- (solid line) and post-contrast spectra (dotted line) from a single voxel are shown at two different resolutions, at $N = 128$ (a) and $N = 32$ (b). At full spectral resolution, the inhomogeneous broadening of the water line is clearly visible. A shoulder on the high-field side of the water resonance is much more clearly resolved after contrast injection (arrow). At the lower resolution, there is significant loss of detail in the water and fat signals, and the effect of the contrast agent is not accurately represented.

Figure 6 shows images that highlight voxels in which there are spectrally inhomogeneous changes caused by contrast agents. The images are calculated at 3 different spectral resolutions, at $N = 128$ (a), 64 (b) and 32 (c). The inhomogeneously broadened pixels tend to appear near the boundary of regions with high water signals: they surround the lesion, and appear along the edges of blood vessels. The number of highlighted voxels is

largest in the image calculated at $N = 128$ - it is 707 vs 593 and 451 in images calculated at $N = 64$ and 32, respectively. However, the random placement of pixels that emerge at full spectral resolution indicates that some of this increase may be due to the increased noise level.

Discussion

Our results suggest that in human breast at 1.5 Tesla, 2.6 Hz spectral resolution or better is required to resolve distinct components of inhomogeneously broadened water resonances (Fig. 4). In addition, very narrow water lines can be accurately measured, providing $T2^*$ contrast within a lesion, which is obscured at lower spectral resolutions (Fig. 3). The intra-lesion inhomogeneities are important for lesion characterization, and thus the obtained $T2^*$ contrast is diagnostically valuable.

Spectrally inhomogeneous effects of contrast agents are resolvable at resolutions of 10.4 Hz or better, allowing a novel approach to the use of contrast agents. While conventional MRI measures only $T1$ and $T2^*$ changes following contrast agent injection, it may be useful to measure changes in water signal lineshape. These effects may be only weakly connected to the changes measured by conventional MRI. In small voxels, the detailed shape of the water resonance is likely to reflect the local magnetic environment and changes in the environment caused by contrast agents. Each resolvable component of the water resonance may represent a different subvoxel population of water molecules in a discrete environment. Thus, changes in resolvable components of the water signal following contrast media injection may reveal details of subvoxel physiology and anatomy that would be difficult or impossible to detect with conventional MRI. For

example, shoulders that appear on the water resonance following contrast media injection may reflect the presence of subvoxelar regions with dense vasculature – and this may be an important marker for cancer. Thus the highest spectral resolution possible, given limitations of SNR and image acquisition time, may provide an important view of the tumor micro-environment. Increases in signal-to-noise ratio due to improved coil design or higher field would allow higher spectral resolution in the future.

Maximum resolution is not optimal for fat suppression. Rather, the FSR is maximized at approximately $N = 32$, after which there is a slight decrease in FSR. Presumably, this is due to the reduced signal-to-noise ratio at higher spectral resolutions. Therefore, for optimal water peak height images, under the present experimental conditions, it may be desirable to smooth the data to a resolution of 5 – 10 Hz, while optimal detection of effects of contrast agents requires higher resolution.

Fitting the fat resonance to a Lorentzian function significantly improves fat suppression (Fig. 2a), allowing detection of small amounts of water in voxels where the fat signal is predominant. This may increase sensitivity to small and/or diffuse cancers. The improvement with fitting of the fat resonance comes from removal of both the wings of signal that may obscure a small water resonance, and the baseline (noise) on which the water signal lies. It is not clear that equivalent results could be achieved with fat saturation. If the fat resonance is homogeneously broadened – then efficient saturation at the center of the resonance would reduce the amplitude of the fat signal all across the spectrum. However, our results point to inhomogeneous broadening: Fig. 2b shows off-

resonance fat signal of magnitude comparable to the water signal. This is consistent with NMR studies of biopsy samples, [39-42] demonstrating that the fat signal represents multiple chemical species with varying chemical shifts. In that case, we can expect high spectral resolution data to yield superior fat suppression.

In conclusion, we have demonstrated that at 1.5 Tesla improvements in fat suppression can be obtained at modest spectral resolution (~ 10 Hz). However, improvements in anatomic detail in tumors, and increased sensitivity to contrast agents, require higher spectral resolution. This higher spectral resolution, combined with high spatial resolution may improve early and accurate detection of breast cancer.

Acknowledgements

This work was supported by grants from the NCI (RO1CA75476 & RO1CA78803), the Army Breast Cancer Research Program (DAMD 17-99-1-9121) and General Electric Medical Systems.

References

1. Soderstrom CE, Harms SE, Farrell RS, Jr., Pruneda JM and Flamig DP, Detection with MR imaging of residual tumor in the breast soon after surgery. *AJR Am J Roentgenol* 1997;168:485-8.
2. Soderstrom CE, Harms SE, Copit DS, et al., Three-dimensional RODEO breast MR imaging of lesions containing ductal carcinoma in situ. *Radiology* 1996;201:427-32.
3. Chen Q, Schneider E, Aghazadeh B, Weinhaus MS, Humm J and Ballon D, An automated iterative algorithm for water and fat decomposition in three-point Dixon magnetic resonance imaging. *Med Phys* 1999;26:2341-7.
4. Wang Y, Li D, Haacke EM and Brown JJ, A three-point Dixon method for water and fat separation using 2D and 3D gradient-echo techniques. *J Magn Reson Imaging* 1998;8:703-10.
5. Daniel BL, Butts K, Glover GH, Cooper C and Herfkens RJ, Breast cancer: gadolinium-enhanced MR imaging with a 0.5-T open imager and three-point Dixon technique. *Radiology* 1998;207:183-90.
6. Szumowski J, Coshov W, Li F, Coombs B and Quinn SF, Double-echo three-point-Dixon method for fat suppression MRI. *Magn Reson Med* 1995;34:120-4.
7. Hardy PA, Hinks RS and Tkach JA, Separation of fat and water in fast spin-echo MR imaging with the three-point Dixon technique. *J Magn Reson Imaging* 1995;5:181-5.
8. Szumowski J, Coshov WR, Li F and Quinn SF, Phase unwrapping in the three-point Dixon method for fat suppression MR imaging. *Radiology* 1994;192:555-61.
9. Glover GH and Schneider E, Three-point Dixon technique for true water/fat decomposition with B₀ inhomogeneity correction. *Magn Reson Med* 1991;18:371-83.
10. Glover GH, Multipoint Dixon technique for water and fat proton and susceptibility imaging. *J Magn Reson Imaging* 1991;1:521-30.
11. Dixon WT, Simple proton spectroscopic imaging. *Radiology* 1984;153:189-94.
12. Nagashima T, Suzuki M, Yagata H, et al., Dynamic-enhanced MRI predicts metastatic potential of invasive ductal breast cancer. *Breast Cancer* 2002;9:226-30.
13. Hayes C, Padhani AR and Leach MO, Assessing changes in tumour vascular function using dynamic contrast-enhanced magnetic resonance imaging. *NMR Biomed* 2002;15:154-63.

14. Liu PF, Debatin JF, Caduff RF, Kacel G, Garzoli E and Krestin GP, Improved diagnostic accuracy in dynamic contrast enhanced MRI of the breast by combined quantitative and qualitative analysis. *Br J Radiol* 1998;71:501-9.
15. Mussurakis S, Gibbs P and Horsman A, Peripheral enhancement and spatial contrast uptake heterogeneity of primary breast tumours: quantitative assessment with dynamic MRI. *J Comput Assist Tomogr* 1998;22:35-46.
16. Kelcz F, Santyr GE, Cron GO and Mongin SJ, Application of a quantitative model to differentiate benign from malignant breast lesions detected by dynamic, gadolinium-enhanced MRI. *J Magn Reson Imaging* 1996;6:743-52.
17. Tofts PS, Berkowitz B and Schnall MD, Quantitative analysis of dynamic Gd-DTPA enhancement in breast tumors using a permeability model. *Magn Reson Med* 1995;33:564-8.
18. Kristoffersen Wiberg M, Aspelin P, Perbeck L and Boné B, Value of MR imaging in clinical evaluation of breast lesions. *Acta Radiol* 2002;43:275-81.
19. Heywang-Köbrunner SH, Bick U, Bradley WG, Jr., et al., International investigation of breast MRI: results of a multicentre study (11 sites) concerning diagnostic parameters for contrast-enhanced MRI based on 519 histopathologically correlated lesions. *Eur Radiol* 2001;11:531-46.
20. Kvistad KA, Rydland J, Vainio J, et al., Breast lesions: evaluation with dynamic contrast-enhanced T1-weighted MR imaging and with T2*-weighted first-pass perfusion MR imaging. *Radiology* 2000;216:545-53.
21. Kacel GM, Liu P, Debatin JF, Garzoli E, Caduff RF and Krestin GP, Detection of breast cancer with conventional mammography and contrast-enhanced MR imaging. *Eur Radiol* 1998;8:194-200.
22. Boné B, Péntek Z, Perbeck L and Veress B, Diagnostic accuracy of mammography and contrast-enhanced MR imaging in 238 histologically verified breast lesions. *Acta Radiol* 1997;38(4) Pt 1:489-96.
23. Boné B, Aspelin P, Bronge L, Isberg B, Perbeck L and Veress B, Sensitivity and specificity of MR mammography with histopathological correlation in 250 breasts. *Acta Radiol* 1996;37:208-13.
24. Kaiser WA, False-positive results in dynamic MR mammography. Causes, frequency, and methods to avoid. *Magn Reson Imaging Clin N Am* 1994;2:539-55.
25. Obdeijn IM, Kuijpers TJ, van Dijk P, Wiggers T and Oudkerk M, MR lesion detection in a breast cancer population. *J Magn Reson Imaging* 1996;6:849-54.
26. Du W, Du YP, Bick U, et al., Breast MR Imaging with High Spectral and Spatial Resolutions: Preliminary Experience. *Radiology* 2002;224:577-85.

27. Yang QX, Demeure RJ, Dardzinski BJ, Arnold BW and Smith MB, Multiple echo frequency-domain image contrast: improved signal-to-noise ratio and T2 (T2*) weighting. *Magn Reson Med* 1999;41:423-8.
28. Karczmar GS, Fan X, Al-Hallaq H, et al., Functional and anatomic imaging of tumor vasculature: high-resolution MR spectroscopic imaging combined with a superparamagnetic contrast agent. *Acad Radiol* 2002;9 Suppl 1:S115-8.
29. Karczmar GS, Fan X, Al-Hallaq HA, et al., Uptake of a superparamagnetic contrast agent imaged by MR with high spectral and spatial resolution. *Magn Reson Med* 2000;43:633-639.
30. Posse S, Wiese S, Gembris D, et al., Enhancement of BOLD-contrast sensitivity by single-shot multi-echo functional MR imaging. *Magn Reson Med* 1999;42:87-97.
31. Sarkar S, Heberlein K, Metzger GJ, Zhang X and Hu X, Applications of high-resolution echoplanar spectroscopic imaging for structural imaging. *J Magn Reson Imaging* 1999;10:1-7.
32. Kovar DA, Al-Hallaq HA, Zamora MA, River JN and Karczmar GS, Fast spectroscopic imaging of water and fat resonances to improve the quality of MR images. *Acad Radiol* 1998;5:269-75.
33. Oikawa H, Al-Hallaq HA, Lewis MZ, River JN, Kovar DA and Karczmar GS, Spectroscopic imaging of the water resonance with short repetition time to study tumor response to hyperoxia. *Magn Reson Med* 1997;38:27-32.
34. Fan X, River JN, Zamora M, et al., Differentiation of nonmetastatic and metastatic rodent prostate tumors with high spectral and spatial resolution MRI. *Magn Reson Med* 2001;45:1046-55.
35. Mansfield P, Spatial mapping of the chemical shift in NMR. *Magn Reson Med* 1984;1:370-386.
36. Doyle M and Mansfield P, Chemical-shift imaging: a hybrid approach. *Magn Reson Med* 1987;5:255-61.
37. Nelson SJ, Vigneron DB, Star-Lack J and Kurhanewicz J, High spatial resolution and speed in MRSI. *NMR Biomed* 1997;10:411-22.
38. Al-Hallaq HA, Fan X, Zamora M, River JN, Moulder JE and Karczmar GS, Spectrally inhomogeneous BOLD contrast changes detected in rodent tumors with high spectral and spatial resolution MRI. *NMR Biomed* 2002;15:28-36.
39. Le Moyec L, Tatoud R, Eugène M, et al., Cell and membrane lipid analysis by proton magnetic resonance spectroscopy in five breast cancer cell lines. *Br J Cancer* 1992;66:623-8.

40. Merchant TE, Kasimos JN, Vroom T, et al., Malignant breast tumor phospholipid profiles using (31)P magnetic resonance. *Cancer Lett* 2002;176:159-67.
41. Merchant TE, Meneses P, Gierke LW, Den Otter W and Glonek T, 31P magnetic resonance phospholipid profiles of neoplastic human breast tissues. *Br J Cancer* 1991;63:693-8.
42. Merchant TE, Thelissen GR, de Graaf PW, Den Otter W and Glonek T, Clinical magnetic resonance spectroscopy of human breast disease. *Invest Radiol* 1991;26:1053-9.

Captions for Illustrations

Figure 1: FSR (a) and S_r (b), calculated at varying N (varying frequency resolution), are shown for five patients with lesions in breast. Crosses represent values obtained without fitting the fat resonance, while the diamonds represent the corrected values obtained using a Lorentzian fit to the fat resonance. For both FSR and S_r , the fitting improves the quality of image.

Figure 2: a) A proton spectrum for a representative voxel containing primarily fat (solid line) and the Lorentzian fit for the fat peak (dashed line) are shown. b) The same spectrum after the Lorentzian fit for the fat signal has been subtracted (solid line) shows the water peak much more clearly. A Lorentzian fit to the water peak is shown (dashed line). Off-resonance components of the fat peak are also evident at ~ 4 ppm. The vertical axis is shown in arbitrary units.

Figure 3: The water (left column) and fat (right column) peak height images of a patient with infiltrating DCIS, calculated using varying echo train lengths: $N = 128$ (a); 32 (b); and 8 (c) are shown. There is improved contrast within the lesion for higher N and corresponding spectral resolution.

Figure 4: The proton spectra in five sample voxels from one patient with infiltrating ductal carcinoma (pixels # 1 - 3) and one healthy volunteer (pixels # 4, 5), measured using varying echo train lengths: $N = 128$ (a); 32 (b); and 8 (c) are shown. The arrow points to shoulders in the water resonance which are not discernible in lower spectral

resolution images. The water peak is placed at 0 ppm in all spectra. The vertical axis is shown in arbitrary units.

Figure 5: The pre- (solid line) and post-contrast (dashed line) spectra from a single voxel are shown at the maximum, $N = 128$ (a), and a lower, $N = 32$ (b) resolution. The arrow points to a shoulder on the water resonance, which is better resolved post-contrast at high resolution, but essentially unchanged in low resolution. The water peak is placed at 0 ppm.

Figure 6: The inhomogeneously broadened pixels are highlighted for images obtained with $N = 128$ (a), 64 (b) and 32 (c).

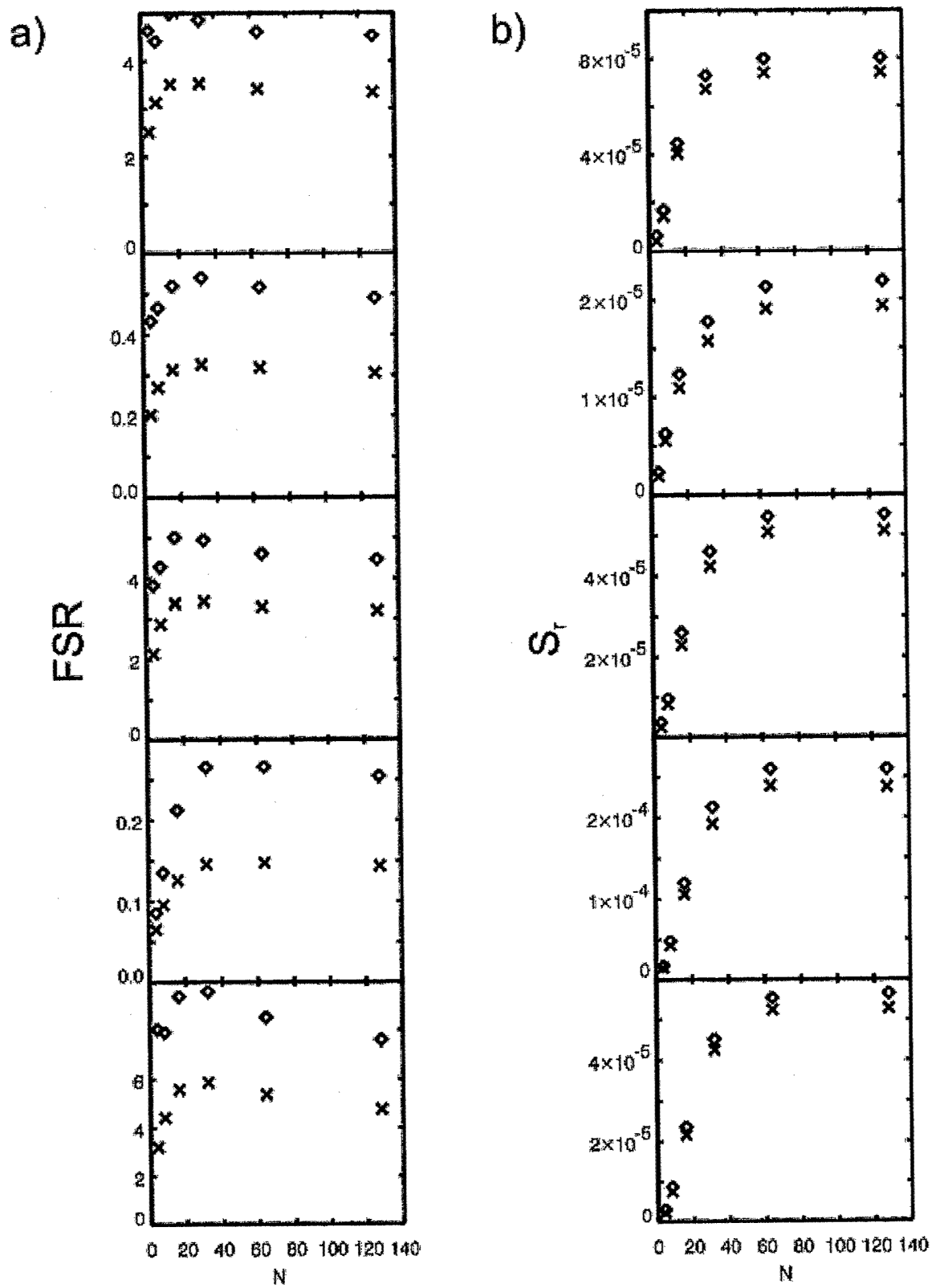


Figure 1

M. Medved et al.

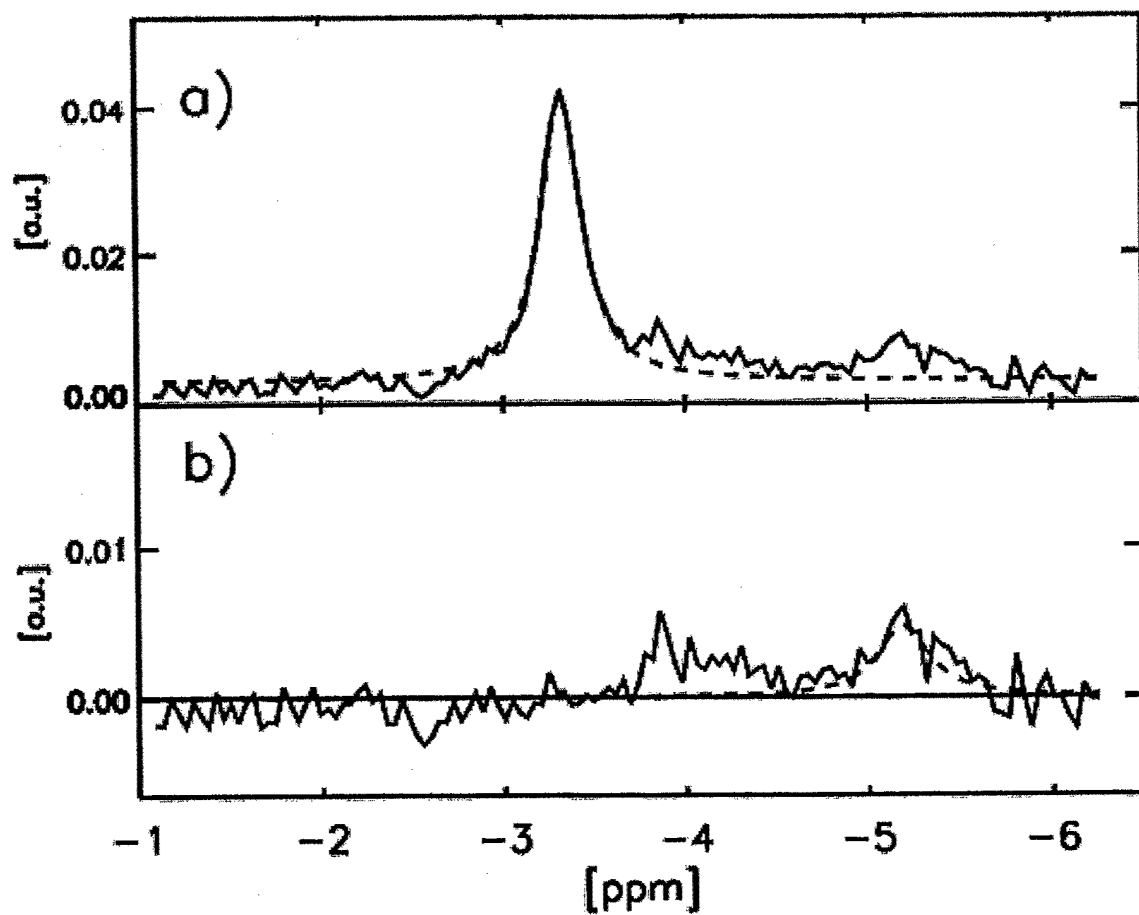


Figure 2

M. Medved et al.

a)

b)

c)

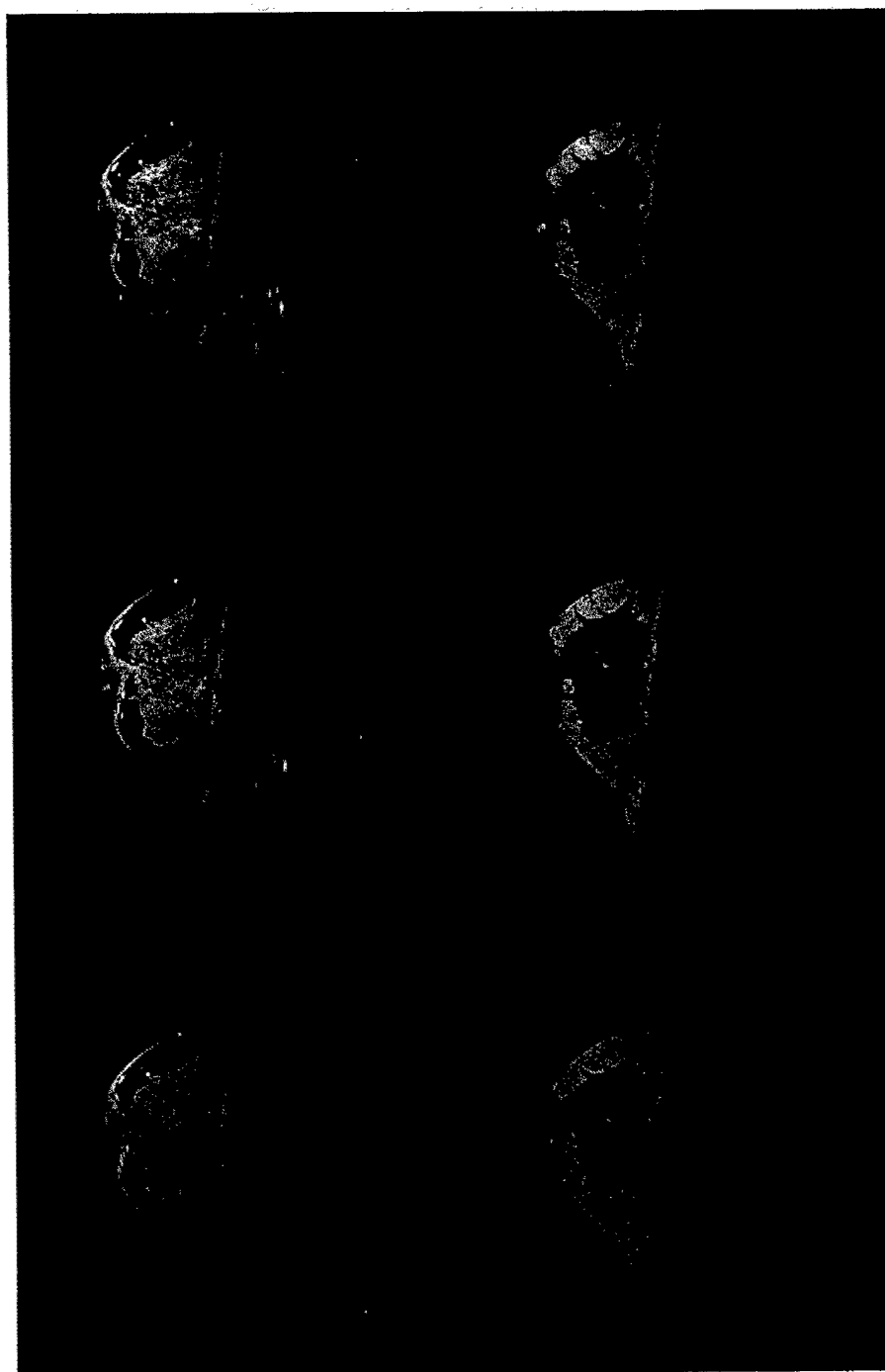


Figure 3

M. Medved et al.

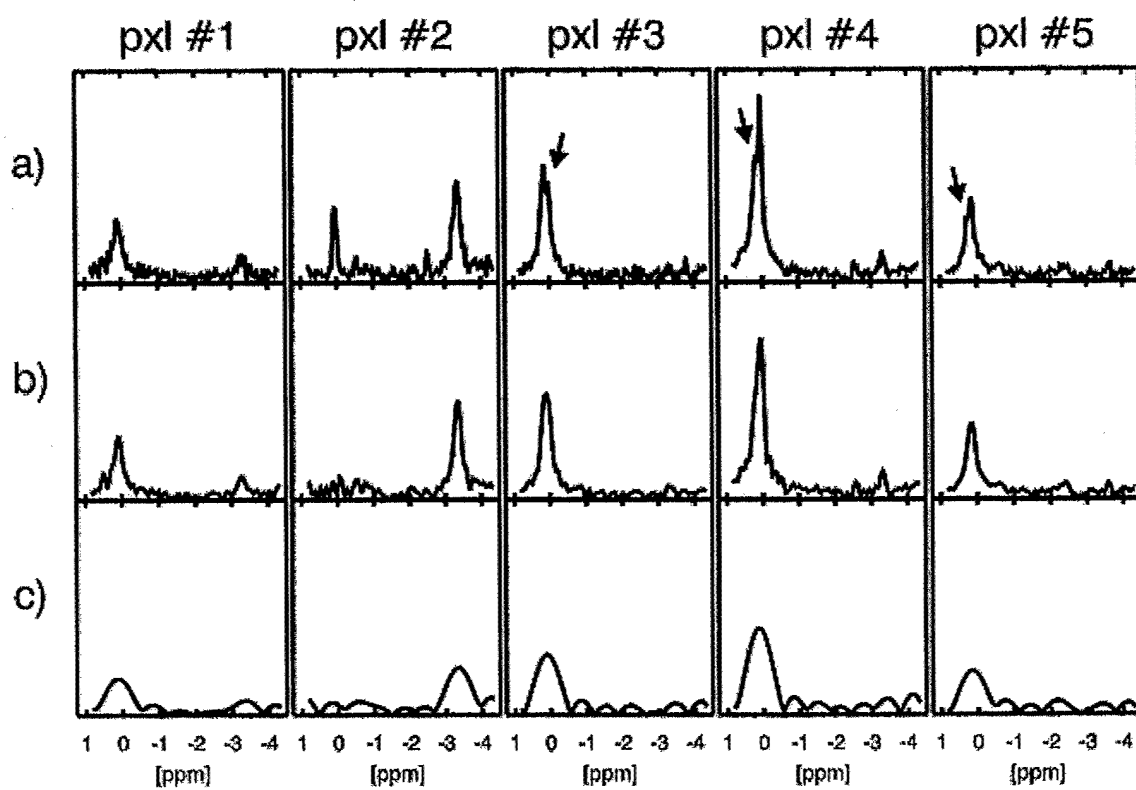


Figure 4

M. Medved et al.

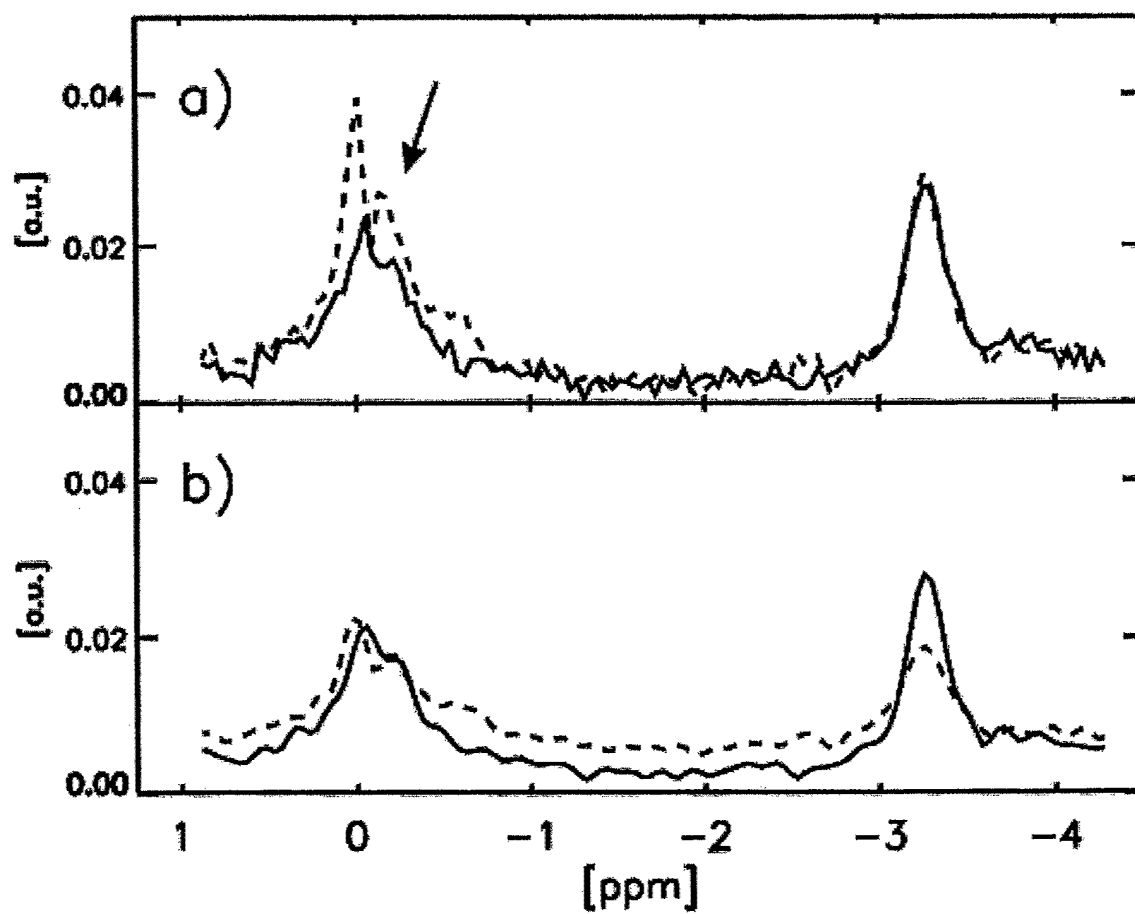


Figure 5

M. Medved et al.

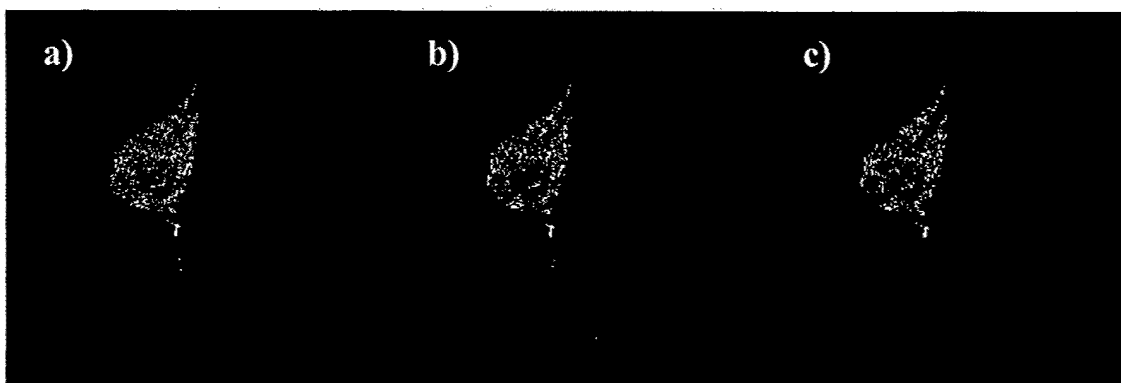


Figure 6

M. Medved et al.

Weiliang Du, MS
Yiping P. Du, PhD
Ulrich Bick, MD
Xiaobing Fan, PhD
Peter M. MacEneaney, FFR,
RCSI
Marta A. Zamora, BA
Milica Medved, PhD
Gregory S. Karczmar, PhD

Index terms:

Breast, MR, 00.121415, 00.121416,
00.12145
Breast neoplasms, calcification, 00.81
Breast neoplasms, diagnosis, 00.32,
00.81
Breast neoplasms, MR, 00.121415,
00.121416, 00.12145

Published online before print

10.1148/radiol.2242011022
Radiology 2002; 224:577-585

Abbreviations:

EPS = echo-planar spectroscopic
HSSR = high spectral and spatial
resolutions
ROI = region of interest

¹ From the Department of Radiology, MC2026, University of Chicago, 5841 S Maryland Ave, Chicago, IL 60637. Received June 11, 2001; revision requested August 3; revision received October 31; accepted December 20. Supported by National Cancer Institute grants RO1CA75476 and RO1CA78803, Army Breast Cancer Research Program grant DAMD 17-99-1-9121, and GE Medical Systems. Address correspondence to G.S.K. (e-mail: gskarczm@midway.uchicago.edu).

© RSNA, 2002

Author contributions:

Guarantors of integrity of entire study, G.S.K., U.B.; study concepts, G.S.K., Y.P.D., U.B., P.M.M.; study design, G.S.K., W.D.; literature research, G.S.K., W.D.; clinical studies, W.D., Y.P.D., P.M.M., U.B., M.A.Z., G.S.K.; experimental studies, W.D., Y.P.D., P.M.M., M.A.Z., M.M., G.S.K.; data acquisition, W.D., Y.P.D., P.M.M., M.A.Z., M.M., G.S.K.; data analysis/interpretation, W.D., X.F., P.M.M., U.B., M.M., G.S.K.; statistical analysis, W.D., X.F., M.M.; manuscript preparation, W.D., X.F., M.M., G.S.K., P.M.M., U.B.; manuscript definition of intellectual content, W.D., Y.P.D., U.B., P.M.M., G.S.K.; manuscript editing, W.D., X.F., M.M., G.S.K.; manuscript revision/review, all authors; manuscript final version approval, G.S.K.

Breast MR Imaging with High Spectral and Spatial Resolutions: Preliminary Experience¹

The authors evaluated magnetic resonance (MR) imaging with high spectral and spatial resolutions (HSSR) of water and fat in breasts of healthy volunteers ($n = 6$) and women with suspicious lesions ($n = 6$). Fat suppression, edge delineation, and image texture were improved on MR images derived from HSSR data compared with those on conventional MR images. HSSR MR imaging data acquired before and after contrast medium injection showed spectrally inhomogeneous changes in the water resonances in small voxels that were not detectable with conventional MR imaging.

© RSNA, 2002

In this article, we describe the use of echo-planar spectroscopic (EPS) imaging for magnetic resonance (MR) imaging of the breast with high spectral and spatial resolutions (HSSR). The goal of this approach is to acquire data with the spatial resolution of typical anatomic images and with a high-resolution spectrum of the water and fat signals for each image pixel. Images calculated from these data sets often provide improved image contrast, anatomic accuracy, and functional information (1-8). HSSR may be particularly useful for MR imaging of the breast because they may improve separation of water and fat signals, contrast, edge delineation, and sensitivity to contrast media and, thus, increase the sensitivity for early carcinomas.

The present application of HSSR MR imaging is a natural extension of previous work that demonstrated the importance of incorporating spectroscopic information into MR images. Dixon first demonstrated that two points of spectral resolution often allow good separation of

water and fat signals (9). Glover and Schneider (10), Glover (11), and others (12,13) produced further improvements in fat-water separation and correction for B_0 inhomogeneity with several points of spectral resolution. More recently, advances in MR hardware and software have allowed rapid acquisition of data with use of EPS MR imaging (14,15) at very high spectral and spatial resolutions.

With EPS MR imaging, details of the water and fat line shapes in each small image pixel can be resolved (4,16) with reasonable acquisition times. HSSR MR imaging is important when the water and fat resonances in small pixels have complicated line shapes. Inhomogeneous broadening due to local magnetic susceptibility gradients is expected on theoretic grounds (17-20) and has been demonstrated experimentally at high spatial resolution (1,3,4,21-23). This effect is especially strong in and near tumors, where deoxygenated blood and a generally heterogeneous environment produce broad complicated water lines (1,22). The detailed structure of the water line can be an important source of information regarding local (subpixel) anatomy and physiology and can be analyzed to improve contrast and accuracy on HSSR MR images (1,24).

The EPS MR imaging approach originally developed by Doyle and Mansfield (14) and Mansfield (15) and subsequently refined by others (25) allows rapid acquisition of HSSR MR imaging data sets. For example, 256×256 matrices in the spatial domain combined with 128-256 points in the spectral dimension and 2-Hz spectral resolution can be acquired in less than 2 minutes with the simplest k-space sampling methods. Much more rapid data acquisition is possible when k space is sampled along two or three axes during readout. Results to date suggest

that the rapidly switching gradients required by EPS MR imaging on clinical MR imagers produce relatively little distortion in proton line shapes, even at resolutions of 1–2 Hz. These results suggest that the effects of eddy currents are relatively small when state-of-the-art self-shielded gradient coils are used (4,6). Thus, it is realistic to consider application of HSSR MR imaging to evaluate suspicious breast lesions in a clinical setting. The purposes of this study were to perform a preliminary evaluation of HSSR MR imaging of the breast and suspicious breast lesions and to compare HSSR MR images with conventional T2-weighted and T1-weighted fat-saturated MR images.

I Materials and Methods

Data Acquisition

Six healthy female volunteers (age range, 28–43 years; mean age, 37 years \pm 5 [mean \pm SD]) and six female patients (age range, 40–61 years; mean age, 47 years \pm 7) were enrolled in this study. The healthy volunteers (ie, women with no history of abnormalities at mammography or palpation) were recruited from among the staff of the radiology department. The patients were recruited through the breast clinic on the basis of having suspicious lesions with a largest diameter of 4 mm to 3 cm on mammograms. All six patients were considered to have high risk of breast cancer. Three patients (selected by U.B.) underwent breast biopsy (performed by the clinical pathology service); one of them was found to have a benign lesion, and the other two were determined to have infiltrating ductal carcinomas. The other three patients did not undergo biopsy. In three of the six patients, abnormalities were not depicted clearly on the conventional MR images, probably because only a limited number of sections were imaged. MR imaging in all subjects was performed according to a protocol approved by the institutional review board after informed consent had been obtained.

The patients underwent MR imaging before and after intravenous injection of a gadolinium chelate (Omniscan; Nycomed Amersham, Princeton, NJ) at a dose of 0.2 mmol per kilogram of body weight. Approximately 20 mL of the contrast media solution was injected by using an automatic injector (Medrad, Pittsburgh, Pa) at a rate of 2 mL/sec. The healthy volunteers did not receive contrast media.

The MR images were acquired with a 1.5-T clinical system (Signa; GE Medical Systems, Milwaukee, Wis) equipped with gradients with a maximum slew rate of 120 mT/m/sec and maximum amplitude of 23 mT/m. Signal was detected by using a dedicated phased-array breast coil, and shimming was performed by using the signal from the entire sensitive volume of the coil. HSSR MR images were acquired with EPS MR imaging sequences. After section selection (section thickness, 4 mm) and phase encoding (256 steps), 128 gradient echoes were acquired by using trapezoidal gradient pulses with alternating polarity. A crusher gradient was applied at the end of the echo train to eliminate artifacts due to residual transverse magnetization. Each gradient echo was sampled at 256 points. The data were digitized at a bandwidth of plus or minus 62.5 kHz, and the time between the centers of gradient echoes was 3.0 msec. The proton free induction decay was sampled for 384 msec, and the repetition time was 500 msec. The resulting data had an in-plane spatial resolution of less than 1 mm (field of view, \leq 24 cm), spectral resolution of 2.6 Hz, and spectral bandwidth of 333 Hz. This bandwidth was sufficient to resolve the water and fat resonances at 1.5 T. Some spectral wrap-around was corrected. Both spectral and spatial resolutions were sufficient to avoid truncation artifacts. Sagittal sections were imaged with the readout gradient applied in the anteroposterior direction to minimize artifacts due to respiratory and cardiac motion.

A T2-weighted multisection fast spin-echo sequence was used to determine locations of suspicious lesions (repetition time msec/echo time msec [effective] of 4,000/176; echo train length, 12; section thickness, 4 mm; matrix, 256 \times 256; field of view, \sim 24 mm; two signals acquired). T1-weighted MR images with fat saturation were acquired with either the fast spin-echo method (600/14 [effective]; echo train length, 12; section thickness, 4 mm; matrix, 256 \times 256; field of view, \sim 24 mm; eight signals acquired) or the conventional spin-echo method (617/14; section thickness, 4 mm; matrix, 256 \times 256; field of view, \sim 24 cm; one signal acquired). HSSR MR images of the selected section were acquired as described earlier, that is, two images before contrast media injection and one image between 1 and 3 minutes after injection. The acquisition time for one HSSR MR image was 128 seconds. T1-weighted fat-saturated MR imaging was repeated at 3 minutes after contrast media injection.

To evaluate the performance of the EPS MR imaging pulse sequence, spherical (\sim 10-cm-diameter) water phantoms containing 10 mmol/L copper sulfate were imaged. The water signal in small voxels in these phantoms (as measured with single-voxel spectroscopy) had a line width of approximately 1–2 Hz. The line width in small voxels of high-resolution spectroscopic images of the phantoms acquired with EPS MR imaging was an accurate indicator of the eddy currents produced by the EPS MR imaging pulse sequence. Eddy currents would significantly broaden the lines and cause phasing artifacts due to frequency shifts during the decay of the free induction decay. EPS MR images were acquired with the same parameters as were used for breast imaging, as described earlier.

Data Analysis and Synthesis of Images

Data analysis was performed with in-house software written in IDL (Interactive Data Language; Research Systems, Boulder, Colo). Raw data generated with EPS MR imaging were processed by using methods described elsewhere (4). In summary, a three-dimensional Fourier transform with respect to two k-space axes and the evolution of the free induction decay provide a data set in which spectral and spatial information are well separated. A high-resolution proton spectrum is associated with each pixel in the image. After the water and fat signals are separated, a variety of images based on the water and fat line shapes can be produced (1,4,8,22,26).

For the purposes of the present study, images were synthesized with signal intensity proportional to the signal peak heights of water and fat (for mixed T2* and T1 contrast), integrals (for T1 contrast), line widths (for T2* contrast), and resonance frequencies. In addition, images were produced to highlight pixels with highly asymmetric water peaks or with multiple resolved components of the water resonance. To represent the effects of contrast media, images were calculated to show changes in peak height, frequency shifts, and spectrally heterogeneous effects.

Separation of Water and Fat Signals

Nonuniformity of the magnetic field across the breast caused variations in the resonance frequencies of water and fat. To identify water and fat signals in each pixel, a frequency map was constructed by using the following algorithm.

1. The largest spectral peak was automatically identified in all image pixels

with signal intensities three times greater than the noise level. A rough frequency map was constructed to represent the resonance frequencies of the identified peaks. This map showed regions that primarily contained water (hereafter, a water region) and regions that primarily contained fat (hereafter, a fat region). The water and fat regions composed most but not all of the breast. Some isolated pixels were not included in either region. Abrupt transitions in resonance frequency of the largest spectral peak (~220 Hz) occurred at the interfaces between water and fat regions. Other sharp transitions equal to the spectral bandwidth (333 Hz) occurred as a result of fold back. Within each region, the frequencies of water or fat were assumed to vary slowly (ie, there were no sharp magnetic field gradients).

2. A seed pixel was manually selected (W.D. and G.S.K. together) in each of one to three fat regions and in each of one to three water regions. Water or fat signals were identified in pixels adjacent to the seed pixel by searching within a narrow bandwidth around the water or fat resonance frequencies in the seed pixel. This process was implemented iteratively by using a region-growing program written (W.D.) in IDL. Within each fat region, the water resonance frequency was calculated in each pixel by using the known fat resonance frequency and the chemical shift offset (+220 Hz). Similarly, the fat resonance frequency was determined in water regions. Fold-back effects were identified on the basis of the sharp change in water or fat resonance frequencies and were corrected by adding or subtracting the spectral bandwidth (333 Hz, or 128 frequency bins) to the frequency of the folded resonance. As a result of this correction, the resonance frequencies for water and fat varied smoothly across all fat and water regions.

3. In pixels outside the fat and water regions—usually pixels with low signal-to-noise ratios—the water and fat resonance frequencies were estimated from the frequency values in the water or fat regions by using a morphologic dilation operation. The gray-value dilation operation was repeatedly applied on the frequency map until the gaps between the water or fat regions were filled, and the water and fat resonance frequencies in all pixels throughout the breast were determined.

The water spectrum was taken to be the signal within plus or minus 10 frequency bins around the central water frequency, as obtained from the frequency

map. To calculate water signal peak height and integral, the water line was fit to the magnitude of a Lorentzian line plus a linear baseline by using a nonlinear least squares curve-fitting algorithm. The water peak height was taken as the highest point of the water line after the baseline was removed with the spectral fitting routine. In principle, this procedure could not precisely fit water lines in many pixels, particularly those that were strongly asymmetric or contained multiple resolved components (23). In practice, however, the fitting procedure provided good approximations for calculation of peak-height and integral images. The procedure allowed accurate detection of a small amount of water, even in the presence of a sloping baseline due, for example, to large fat signals with broad wings or signals that leaked from other voxels.

Texture Analysis

Image texture was measured in a region of interest (ROI) selected to include as much as possible of the breast but to exclude the chest wall. ROIs were selected manually by MR physicists (X.F. and W.D. together) with advice from a radiologist (P.M.M. or U.B.). Image signal intensity in the ROI was normalized by the average value of image signal intensity in the ROI so that images from different examinations could be compared. Image signal intensity was expressed as a function (f) of the column (x) and row (y) index for each pixel. Mathematically, $f(x, y)$ represents a surface spanning an ROI on an image coordinate plane x - y . The area of the surface, S , was found from

$$S = \sum \sqrt{1 + f_x^2 + f_y^2} \quad (1)$$

where the summation is over the ROI, $f_x = \delta f / \delta x$, and $f_y = \delta f / \delta y$. We defined the normalized surface area (S_r) as

$$S_r = 100.0 \cdot |S(\text{ROI}) - S_{xy}| / S'_{xy} \quad (2)$$

where $S(\text{ROI})$ is the surface area calculated from Equation (1) and S_{xy} is the area of $S(\text{ROI})$ projected onto the x - y plane. Thus, S_r is a measure of the variation or roughness in image signal intensity (eg, if the image signal intensity is constant, then S_r is 0.0).

Locating Pixels with Multiple Peaks and Asymmetric Peaks

Multiple peaks and asymmetric peaks were identified automatically with software written in IDL. To find the number of resolved peaks in the water resonance

in each pixel, all possible peaks in the water line were automatically located with the software (ie, those points in the spectrum where the signal was larger than that at the adjacent points). Then, with the program, spectral amplitude was measured at the local minima between these candidate peaks. Candidate peaks were selected as true peaks if the difference between the local maximum and minimum was two times larger than the root-mean-square of the noise level. The number of resolved peaks was counted for each pixel, and images were constructed to show the location of pixels that contained multiple water peaks.

To determine the asymmetry of magnitude spectra, the sides of the spectra on either side of the global maxima were compared. Spectra were identified as asymmetric if the difference between the integrals of the high- and low-frequency sides of the resonance was larger than 10% of the total integral.

Analysis of Effects of Contrast Media on HSSR Data

Before the effects of contrast media were evaluated, the HSSR data sets were corrected for motion in two dimensions. In-plane breast motions, including translation, rotation, and scaling, were modeled with a six-parameter coordinate transform. The postcontrast peak-height image was taken as the reference to which the precontrast peak-height image was registered. Six to 12 corresponding points that represented shared anatomic features were manually identified on the two peak-height images. The parameters of the coordinate transform were determined by minimizing the squared difference between the coordinates of the corresponding points. Finally the coordinate transform and bilinear interpolation were applied to obtain the motion-corrected precontrast HSSR data set.

Software was written in IDL to measure the change in the water signal integral, peak height, frequency, and $T2^*$ caused by the contrast media. The integral of the water magnitude spectrum before contrast media injection was subtracted from that after contrast media injection. The frequency shift due to the contrast media in each pixel was calculated after zero filling of the free induction decays to 2,048 points. $T2^*$ was estimated by dividing the peak height by the peak integral of the water spectrum for each pixel. The changes in $T2^*$ due to the contrast media were then computed.

To study the spectrally inhomogeneous

effects of the contrast media (1,3,4,8, 22,26), images were generated on the basis of the difference spectrum obtained by subtracting the precontrast spectrum in each pixel from the postcontrast spectrum. Both the pre- and postcontrast free induction decays were zero filled to 512 points before being Fourier transformed. The postcontrast spectrum from each pixel was then shifted until the absolute difference between the pre- and postcontrast spectra was minimized. This shift corrected for contrast media-induced changes in bulk susceptibility that shifted the entire water signal. The resulting difference spectra were used to synthesize images on which signal intensity was proportional to the greatest positive and negative amplitudes in the difference spectra and also to the greatest absolute change in spectral amplitude in each pixel. In addition, we synthesized images proportional to the product of absolute values of the greatest positive and negative changes in the difference spectrum.

Evaluation by Experienced Radiologists

The conventional and HSSR MR images of the breast in all subjects ($n = 12$) were reviewed independently by two radiologists (U.B. and P.M.M., who have 10 and 5 years of experience, respectively). The radiologists were provided with the medical histories including the mammographic findings, if any, but excluding the biopsy results. The radiologists evaluated the diagnostic usefulness of the HSSR MR images over that of the conventional images in terms of the separation of fat and water signals, the depiction of normal tissues, lesions, and surrounding vascular structures, and the sensitivity of the imaging technique to the contrast media.

Statistical Analysis

Nonparametric (Wilcoxon signed-rank) tests were performed with commercially available software (Minitab, State College, Pa) with data from the normal breasts. The tests were performed to compare the effectiveness of fat suppression and image texture or sharpness on water HSSR MR images and conventional T1-weighted fat-saturated MR images. Differences with $P \leq .05$ were considered statistically significant.

1 Results

Accurate high-resolution spectroscopic imaging with EPS MR imaging requires

that the gradient waveforms be produced with minimal eddy currents and that shimming is adequate. EPS MR imaging of water phantoms produced narrow (≤ 2 -Hz) symmetric water lines with no phasing artifacts. These images demonstrated that eddy current and shimming effects were small and did not distort spectra, even at resolution of less than 2 Hz.

The high-resolution EPS MR images demonstrated strong spectral inhomogeneity of water signal line shapes in the breast. Water signals from individual small voxels often contained multiple resolved components or were clearly asymmetric. For example, the water resonance in $12.5\% \pm 9.0$ (mean \pm SD) of all pixels in six normal breasts was composed of two or more multiple resolved components. A larger percentage of pixels in these breasts contained asymmetric pixels: $20.4\% \pm 10.8$. These parameters were similar in the group of women with breast lesions: $20.7\% \pm 8.2$ of pixels contained water resonances with multiple resolved components and $30.7\% \pm 10.9$ contained asymmetric resonances.

These percentages are based on the total number of pixels in the breast and, thus, are low owing to the fact that some pixels do not contain detectable water. In pixels that contained a significant amount of MR-detectable water, approximately $30.4\% \pm 6.3$ of the water resonances contained multiple resolved components. After contrast media injection ($n = 6$), $16.9\% \pm 8.8$ of pixels in the breasts contained water signals with multiple resolved components. The spectral inhomogeneity of the water resonance is illustrated in Figure 1. An image synthesized from water signal peak height and representative spectra acquired before and after contrast media injection from selected pixels is shown. Inhomogeneous broadening of the water peak is clear in many of the spectra, and some water resonances have two or more resolvable components (spectra 3, 4, 5, and 7). The response of the water resonance to the contrast media is different from that of the fat resonance. In spectrum 1, for example, the water peak shifts to higher frequency and its magnitude increases, while the fat peak does not shift and its magnitude decreases slightly. In spectra 4, 5, and 7, the contrast agent produces a well-defined shoulder or fully resolved component on the high-frequency side (low-field-strength side) of water. The increases in overall peak height of the water signal are expected because the acquisitions are T1 weighted.

Inhomogeneous broadening of the water resonance can be used to produce images that highlight anatomic features. For one of the breasts imaged, the spatial distribution of pixels with non-Lorentzian water spectra is illustrated in Figure 2, which highlights pixels in which the water resonance has multiple components (Fig 2, B) or is asymmetric (Fig 2, C). In this breast, the water resonances in approximately 21% of the tumor pixels contain two or more resolved components, and the spectra in 39% of pixels are asymmetric. Pixels with complicated water resonances tended to be near the tumor edges or near large vessels.

Although asymmetry and multiple resolved components are clear indicators of inhomogeneous broadening, even relatively symmetric water resonances are often inhomogeneously broadened. Spectral inhomogeneity is clear from the effects of contrast media on distinct components of relatively symmetric water resonances (eg, spectra 3, 4, 5, and 7 in Fig 1). The effects of contrast media in many pixels were spectrally inhomogeneous, that is, the changes caused by the contrast media were not uniform across the water spectrum. The largest change in the spectrum was often not at the center of the water resonance.

To evaluate fat suppression on water HSSR MR images, the signal in parenchymal pixels on these images (ie, pixels that primarily contained water) was divided by the signal in pixels that primarily contained fat. This ratio is referred to as the fat-suppression ratio in the following data. The fat-suppression ratios were significantly higher (Wilcoxon signed-rank test, two-tail $P = .036$) on water HSSR MR images (3.7 ± 0.1 [mean \pm standard error of the mean]) than on T1-weighted fat-saturated images (1.4 ± 0.2). Regions of insufficient fat suppression on the conventional images were evident, but in addition the general background in predominantly fat regions on conventional fat-saturated MR images was brighter than that on water HSSR MR images. This difference is illustrated in Figure 3, which shows conventional and HSSR MR images of single sagittal sections in six healthy breasts.

Improved fat suppression on water HSSR MR images enhances contrast in the parenchyma. The Table shows quantitative comparisons of the T1-weighted fat-saturated MR images and water HSSR MR images presented in Figure 3. Because the signal-to-noise ratios were similar on HSSR and T1-weighted MR images (Table), the normalized surface area (S , in Eq

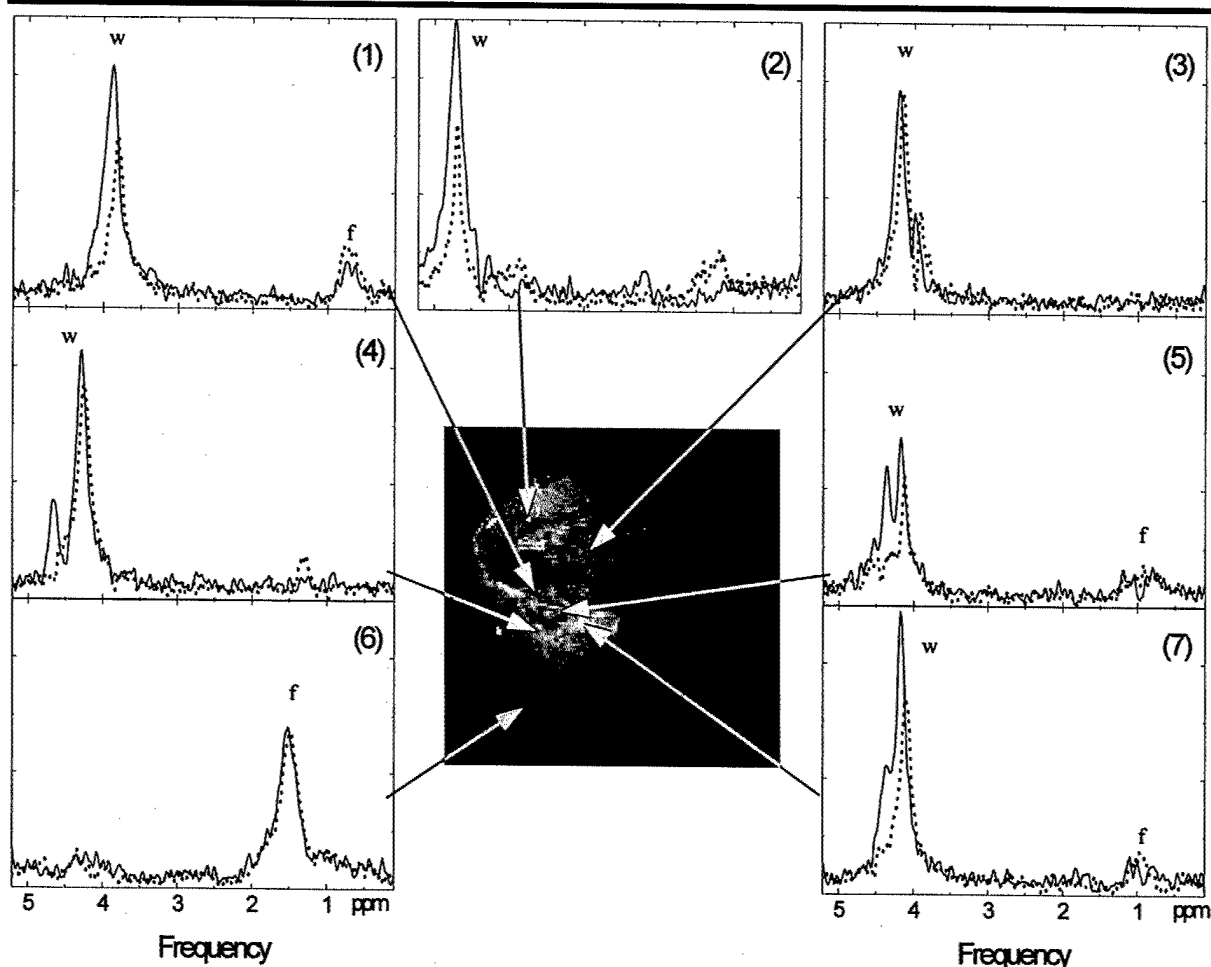


Figure 1. Representative spectra from selected pixels before (dotted lines) and after (solid lines) contrast medium injection. Reference image shows a sagittal section through a breast with ductal carcinomas (sampled with spectra 1, 4, 5, and 7). All spectra are on the same scale and are referenced to the same carrier frequency. Frequency shifts due to B_0 variation across the breast are apparent. The water peak (*w*) and fat peak (*f*) are labeled for each spectrum. Spectra in some pixels have approximately the same shape before and after contrast media injection (spectra 1, 2, 3, and 6), which indicates that effects of interimage motion have been minimized.

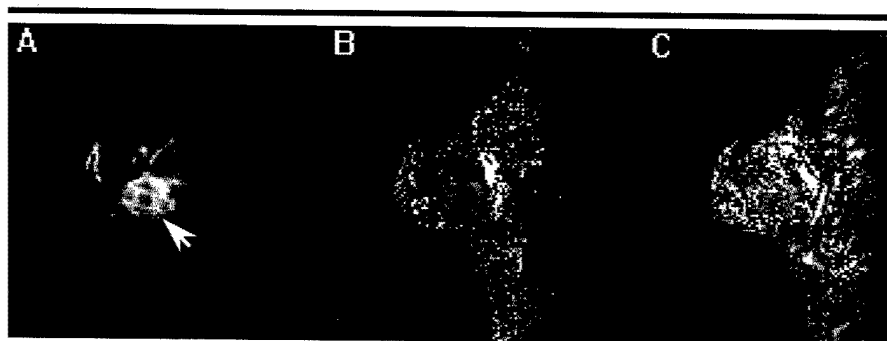


Figure 2. A, Pixels with non-Lorentzian spectral shapes are overlaid on a sagittal reference water peak-height HSSR MR image of a breast with a lesion (arrow). B, Pixels in which the water resonance contains multiple resolved peaks are highlighted. Only peaks with signal-to-noise ratio of at least 2 were identified as secondary peaks. C, Pixels with strongly asymmetric water resonances are highlighted.

[2]) can be used to compare texture and sharpness (S_s) of the HSSR MR images with those of the T1-weighted MR images. S_s values, tabulated in the Table, are

larger (Wilcoxon signed-rank test, two-tailed $P = .036$) on water HSSR MR images than those on T1-weighted MR images. The results demonstrate that HSSR

MR images generally provide better fat-water separation and better contrast and texture compared with those on conventional T1-weighted MR images with fat saturation.

Strong enhancement was found on MR images obtained in the two patients with histopathologically proved invasive ductal carcinomas. Two experienced radiologists (blinded independent evaluation by U.B. and P.M.M.) agreed that image contrast was improved on HSSR MR images compared with that on conventional images and that tumor boundaries were more clearly defined. Fat signal was more effectively suppressed on the water HSSR MR images so that the water-containing structures were clearly seen against a dark background. These findings are illustrated in Figure 4, where conventional and HSSR MR images are compared. The contrast ratio for the first lesion (arrow in

part A) compared with surrounding tissue (average signal in lesion divided by average signal in surrounding tissue) is 4.4 on the water peak-height HSSR MR image before contrast media injection (part C), 4.8 after contrast media injection (part D), and 1.9 on the T1-weighted fat-saturated MR images after injection (part B). The vascular network (arrow in part D) in the first breast is better depicted on HSSR MR images. Further, U.B. and P.M.M. found that the edges of the second lesion (arrow in part E) are more clearly delineated on peak-height HSSR MR images than on conventional MR images, especially near the chest wall (arrow in part H). In this case, HSSR MR images provide a clearer view of whether or not the lesion is infiltrating the chest wall.

The effects of contrast agents on water signal line shape and resonance frequency can be used to produce novel images. For example, Figure 5 illustrates the effects of contrast media on HSSR data sets. Figure 5, A shows changes on an image derived from the first gradient echo of the EPS echo train (postcontrast image minus precontrast image). This image simulates the effect of the contrast media on conventional T1-weighted gradient-echo MR images. Strong signal enhancement is seen in blood vessels at the tumor rim and in some pixels inside the tumor. Figure 5, B shows the change in the water peak-height image. The inherent T2* weighting in this image shows regions of decreased or increased signal intensity. Figure 5, C shows a map of the water peak-frequency change after contrast media injection. These changes were greatest in large vessels. Frequency changes are evident in elongated structures in the tumor interior that perhaps indicate the primary veins and arteries in the tumor center. Finally, image signal intensity in Figure 5, D is proportional to the product of the absolute values of the largest positive and negative changes in the water spectrum. This product image highlights pixels with spectrally heterogeneous contrast media effects and shows changes beyond the edge of the upper quadrant of the lesion that are not clear on the conventional image (Fig 5, A). The images derived from HSSR data show strong features that are not evident on conventional images (Fig 4, A, B).

Discussion

These preliminary results demonstrate the application of HSSR imaging to human breast MR imaging and evaluation of suspicious lesions. We evaluated both

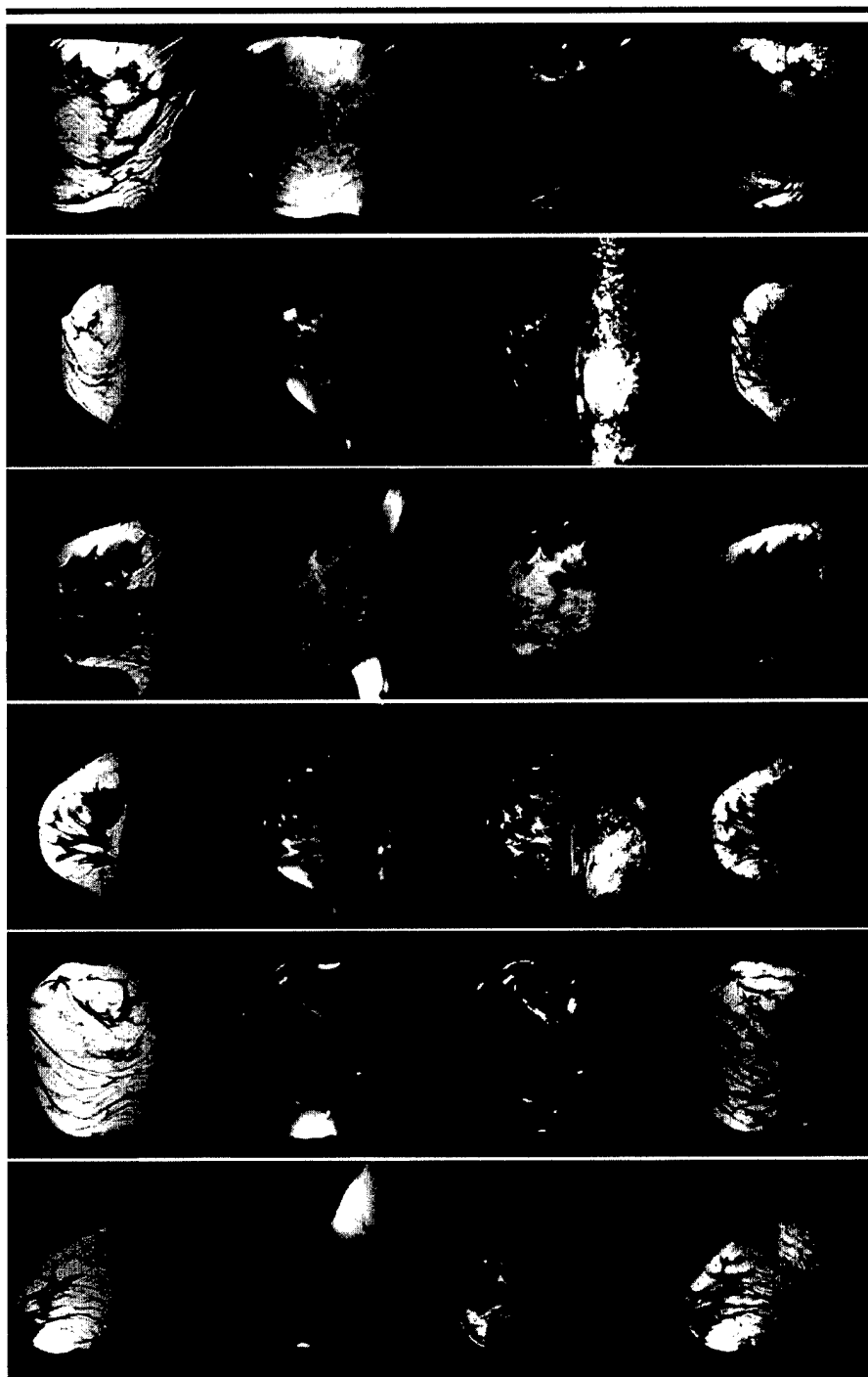


Figure 3. Conventional and HSSR MR images of six healthy breasts. For each breast (one row), four sagittal images are shown. From left to right: T2-weighted fast spin-echo MR images, T1-weighted fat-saturated fast spin-echo MR images, water peak-height HSSR MR images, and fat peak-height HSSR MR images. Image signal intensities are adjusted to a similar level, and images are displayed with identical window settings. Conventional and HSSR MR images were each acquired in approximately 1.5–2.0 minutes.

conventional properties (ie, contrast, texture, and fat suppression) and image characteristics obtained from high-resolution spectral information that is available only with HSSR MR imaging. In both cases, our results suggest that HSSR MR

imaging has some advantages over conventional MR imaging. Results of both quantitative analysis and evaluations by experienced radiologists suggest that HSSR MR images may show anatomy that is more clearly defined than that on con-

Comparison of Fat-Suppression Ratio, Normalized Surface Area, and Signal-to-Noise Ratio in Six Normal Breasts

Patient No.	Fat-Suppression Ratio*		Normalized Surface Area†		Signal-to-Noise Ratio	
	T1-weighted Fat-saturated MR Images	HSSR MR Images	T1-weighted Fat-saturated MR Images	HSSR MR Images	T1-weighted Fat-saturated MR Images	HSSR MR Images
1	0.9	3.5	0.6	4.9	13	12
2	1.2	3.7	1.4	12.1	31	29
3	1.6	4.2	0.5	1.3	14	30
4	1.5	3.4	2.2	5.8	13	12
5	1.1	3.5	3.2	16.6	26	26
6	2.3	4.0	5.5	5.6	37	27
Mean \pm standard error of the mean	1.4 \pm 0.2	3.7 \pm 0.1	2.2 \pm 0.8	7.7 \pm 2.3	22.3 \pm 4.3	22.7 \pm 3.4

* Fat-suppression ratio = signal in parenchymal pixels containing primarily water divided by signal in pixels containing primarily fat.

† Definition of normalized surface area is given by S_f in Equation (2). S_f is designed to measure the sharpness of an image.

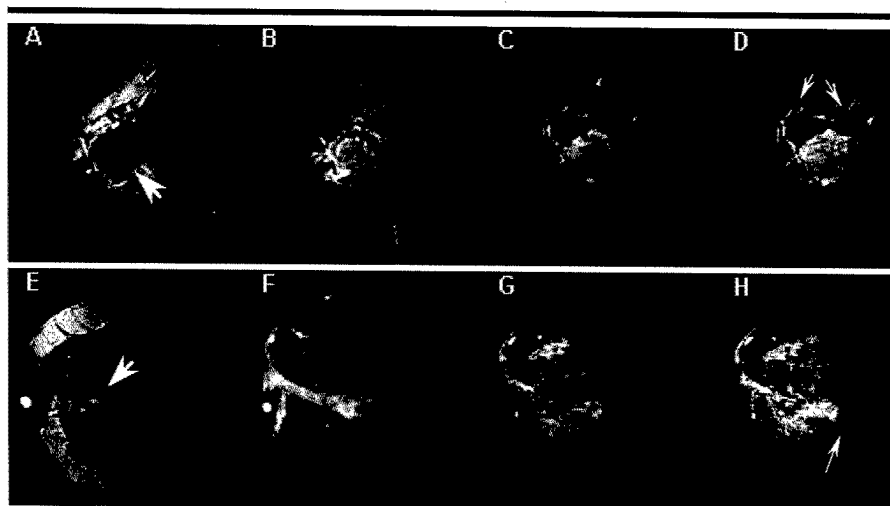


Figure 4. A-H, Sagittal images of breasts with carcinomas (arrows). Top row: Images in a 47-year-old patient with infiltrating ductal carcinoma, Scarff-Bloom-Richardson grade II, in the left breast. Bottom row: Images in a 47-year-old patient with infiltrating ductal carcinoma, Scarff-Bloom-Richardson grade II, with a moderate component of ductal carcinoma in situ, low grade, in the right breast. A and E are T2-weighted fast spin-echo MR images before contrast medium injection. B and F are T1-weighted fat-saturated MR images acquired 3 minutes after contrast medium injection. C and G are HSSR MR images proportional to water resonance peak height before contrast medium injection. D and H are water peak-height images obtained 1-3 minutes after the contrast medium injection. Evaluation by experienced radiologists suggested that vasculature and lesion edges are more clearly delineated on the HSSR MR images (C, G).

ventional MR images. The HSSR MR images (eg, Fig 4) show well-defined lesion boundaries, which are important clinically because irregular lesion contours are a sign of malignancy (27,28). In addition, detailed spectral data allowed accurate fitting of the water peak and separation of the water signal from the spectral baseline. As a result, small water signals could be accurately detected in the presence of very large fat signals, even when the wings of fat spectra extended into the water region, owing to very rapid decay in the time domain. The improved separation of the water and fat signals increases sensitivity to small amounts of

water, and this increase may facilitate detection of cancer.

The HSSR MR images were acquired 1-3 minutes after contrast media injection, whereas the conventional T1-weighted fat-saturated MR images were acquired 3-5 minutes after injection, which caused some bias in favor of HSSR MR images. However, there was no data acquisition at the peak of the contrast media bolus; both HSSR and conventional MR images were acquired during a period after the peak enhancement is usually reached, and signal intensity changes during this period are generally slow. Therefore, comparison of the HSSR

and conventional MR images acquired after contrast media injection is reasonable.

The HSSR data demonstrate that the water line in breast tissue is inhomogeneously broadened and often contains multiple resolved components. It is very unlikely that this spectral inhomogeneity is a consequence of poor shimming. In these very small image pixels, magnetic field gradients due to shimming are approximately linear and, therefore, broaden the water line but do not cause detectable asymmetry or multiple resolved components. Spectrally inhomogeneous effects of the contrast media were detected in many pixels; this finding is consistent with those in previous studies of animal models of cancer (1,3,8,22) and with theoretic predictions (17,19,20).

We sometimes found strong but opposing changes in the amplitudes of different spectral components in the same image pixel. Thus, high spectral resolution makes it possible to detect strong effects of contrast media that are missed with conventional MR imaging. Large changes in a single small component of an inhomogeneously broadened resonance may reflect subpixel regions of high vascular density associated with angiogenesis. This hypothesis is consistent with the fact that spectrally inhomogeneous contrast media effects appear to cluster near the edges of tumors, where strong angiogenic activity is expected (Fig 5, D; references 1 and 3).

With the current relatively slow method of data acquisition, high-resolution EPS MR images may be useful for improved characterization of suspicious lesions identified with conventional MR imaging or other modalities. However, much faster versions of the method can be implemented that involve the use of two- or three-dimensional trajectories through k

space during the proton free induction decay (15). Other methods for more efficient and rapid data acquisition are also available. Methods (eg, simultaneous acquisition of spatial harmonics [29]) for parallel data acquisition can dramatically increase speed, and spectral resolution can be reduced at the edges of k space. Thus, it is likely that high-quality HSSR MR images can be obtained more rapidly or from a large volume of tissue with adequate signal-to-noise ratio.

A definitive evaluation of HSSR MR imaging would include direct comparison with optimal multiple-point Dixon methods (9–11), optimal fat-suppression methods (eg, rotating delivery of excitation off resonance [30]), and other MR imaging methods (eg, magnetization transfer contrast material-enhanced MR imaging [31]). Such an evaluation is feasible since EPS MR imaging or related methods are available in a number of laboratories where they are used to improve the accuracy and sensitivity of anatomic and functional MR imaging (2,4,7,18,21,32–34). In addition, the hardware and software required to produce HSSR EPS data sets are either commonly available or can be implemented easily. Thus, more comprehensive clinical testing of this approach for MR imaging of the breast is practical.

In conclusion, these preliminary results, as well as findings in previous work (1,3,6–8,22,24,26,33), suggest potential advantages of HSSR MR imaging of the breast. Advantages of HSSR MR imaging include improved anatomic accuracy and edge delineation, improved fat suppression, increased sensitivity to small amounts of water-containing tissue, strong T2* contrast, increased sensitivity to contrast media, and increased sensitivity to subpixel environments (1,3). Future improvements in HSSR MR imaging will reduce data acquisition time. Even without these improvements, we believe the information provided with HSSR MR imaging may justify the longer acquisition times.

Acknowledgments: G.S.K. is grateful for the very helpful advice of Dr Alan Koretsky, Dr Frederick Kelcz, Dr Edward Hendrick, and Dr Martin Lipton.

References

1. Karczmar GS, Fan X, Al-Hallaq HA, et al. Uptake of a superparamagnetic contrast agent imaged by MR with high spectral and spatial resolution. *Magn Reson Med* 2000; 43:633–639.
2. Yang QX, Demeure RJ, Dardzinski BJ, Arnold BW, Smith MB. Multiple echo frequency-domain image contrast: improved signal-to-noise ratio and T2

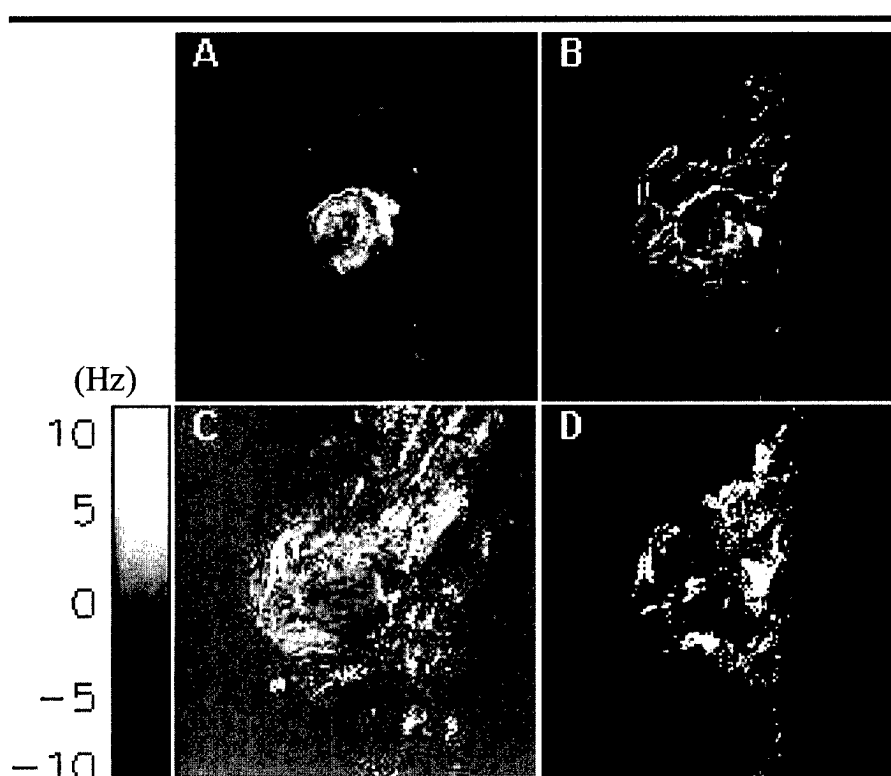


Figure 5. Effects of contrast medium on HSSR MR images. These sagittal images were obtained of the lesion shown in Figure 4, A–D. A, Changes in the image synthesized from the first echo in the HSSR echo train are depicted. This image simulates a conventional T1-weighted subtraction MR image. B, Changes in peak height of the water magnitude spectra are depicted. C, Changes in water resonance frequency (in hertz) are depicted. Increase in frequency gives rise to higher signal on the image. D, Pixels are highlighted in which the difference spectra (postcontrast spectrum minus precontrast spectrum) show spectrally heterogeneous changes.

- (T2*) weighting. *Magn Reson Med* 1999; 41:423–428.
3. Karczmar G, Fan X, Al-Hallaq H, et al. Functional and anatomic imaging of tumor vasculature: high resolution MR spectroscopic imaging combined with a superparamagnetic contrast agent. *Acad Radiol* 2002; 9(suppl 1):S115–S118.
4. Kovar DA, Al-Hallaq HA, Zamora MA, River JN, Karczmar GS. Fast spectroscopic imaging of water and fat resonances to improve the quality of MR images. *Acad Radiol* 1998; 5:269–275.
5. Kuperman V, River JN, Karczmar GS. High resolution spectroscopic images of tumors (abstr). In: Proceedings of the Society of Magnetic Resonance in Medicine and the European Society of Magnetic Resonance in Medicine and Biology. Berkeley, Calif: Society of Magnetic Resonance in Medicine, 1995.
6. Sarkar S, Heberlein K, Metzger GJ, Zhang X, Hu X. Applications of high-resolution echoplanar spectroscopic imaging for structural imaging. *J Magn Reson Imaging* 1999; 10:1–7.
7. Posse S, Wiese S, Gembris D, et al. Enhancement of BOLD-contrast sensitivity by single-shot multi-echo functional MR imaging. *Magn Reson Med* 1999; 42:87–97.
8. Oikawa H, Al-Hallaq HA, Lewis MZ, River JN, Kovar DA, Karczmar GS. Spectroscopic imaging of the water resonance with short repetition time to study tumor response to hyperoxia. *Magn Reson Med* 1997; 38:27–32.
9. Dixon WT. Simple proton spectroscopic imaging. *Radiology* 1984; 153:189–194.
10. Glover GH, Schneider E. Three-point Dixon technique for true water/fat decomposition with B0 inhomogeneity correction. *Magn Reson Med* 1991; 18:371–383.
11. Glover GH. Multipoint Dixon technique for water and fat proton and susceptibility imaging. *J Magn Reson Imaging* 1991; 1:521–530.
12. Szumowski J, Coshov WR, Li F, Quinn SF. Phase unwrapping in the three-point Dixon method for fat suppression MR imaging. *Radiology* 1994; 192:556–561.
13. Wang Y, Li D, Haacke EM, Brown JJ. A three-point Dixon method for water and fat separation using 2D and 3D gradient-echo techniques. *J Magn Reson Imaging* 1998; 8:703–710.
14. Doyle M, Mansfield P. Chemical shift imaging: a hybrid approach. *Magn Reson Med* 1987; 5:255–261.
15. Mansfield P. Spatial mapping of the chemical shift in NMR. *Magn Reson Med* 1984; 1:370–386.
16. Kovar DA, Lewis MZ, River JN, Lipton MJ, Karczmar GS. In vivo imaging of extraction fraction of low molecular weight MR contrast agents and perfusion rate in ro-

- dent tumors. *Magn Reson Med* 1997; 38: 259-268.
17. Chu SC, Xu Y, Balschi JA, Springer CSJ. Bulk magnetic susceptibility shifts in NMR studies of compartmentalized samples: use of paramagnetic reagents. *Magn Reson Med* 1990; 13:239-262.
18. Xu Y, Balschi JA, Springer CSJ. Magnetic susceptibility shift selected imaging: MESSI. *Magn Reson Med* 1990; 16:80-90.
19. Bauer WR, Nadler W, Bock M, et al. Theory of the BOLD effect in the capillary region: an analytical approach for the determination of T2 in the capillary network of myocardium. *Magn Reson Med* 1999; 41:51-62.
20. Yablonskiy DA. Quantitation of intrinsic magnetic susceptibility-related effects in a tissue matrix: phantom study. *Magn Reson Med* 1998; 39:417-428.
21. Zhong K, Li X, Shachar-Hill Y, Picart F, Wishnia A, Springer CSJ. Magnetic susceptibility shift selected imaging (MESSI) and localized $(1)H(2)O$ spectroscopy in living plant tissues. *NMR Biomed* 2000; 13:392-397.
22. Al-Hallaq HA, Zamora M, Fish BL, Farrell A, Moulder JE, Karczmar GS. MRI measurements correctly predict the relative effect of tumor oxygenating agents on hypoxic fraction in rodent BA1112 tumors. *Int J Radiat Oncol Biol Phys* 2000; 47:481-488.
23. Al-Hallaq HA, Fan X, Zamora M, River JN, Moulder JE, Karczmar GS. Spectrally inhomogeneous BOLD contrast changes detected in rodent tumors with high spectral and spatial resolution MRI. *NMR Biomed* 2002; 15:28-36.
24. Kovar DA, Lewis M, Karczmar GS. A new method for imaging perfusion and contrast extraction fraction: input functions derived from reference tissues. *J Magn Reson Imaging* 1998; 8:1126-1134.
25. Nelson SJ, Vigneron DB, Star-Lack J, Kurhanewicz J. High spatial resolution and speed in MRSI. *NMR Biomed* 1997; 10:411-422.
26. Al-Hallaq HA, Karczmar G. High resolution $1H$ spectroscopic imaging of the water and fat resonances in human breast (abstr). In: Proceedings of the Fifth Meeting of the International Society for Magnetic Resonance in Medicine. Berkeley, Calif: International Society for Magnetic Resonance in Medicine, 1997; 1055.
27. Schnall MD, Ikeda DM. Lesion Diagnosis Working Group report. *J Magn Reson Imaging* 1999; 10:982-990.
28. Orel SG, Schnall MD, LiVolsi VA, Troupin RH. Suspicious breast lesions: MR imaging with radiologic-pathologic correlation. *Radiology* 1994; 190:485-493.
29. Bankson JA, Griswold MA, Wright SM, Sodickson DK. SMASH imaging with an eight element multiplexed RF coil array. *MAGMA* 2000; 10:93-104.
30. Soderstrom CE, Harms SE, Copit DS, et al. Three-dimensional RODEO breast MR imaging of lesions containing ductal carcinoma in situ. *Radiology* 1996; 201:427-432.
31. Balaban R, Ceckler TL. Magnetization transfer contrast in magnetic resonance imaging. *Magn Reson Q* 1992; 8:116-137.
32. Kovar DA, Karczmar GS. Fast spectroscopic imaging of water and fat proton resonances improves image contrast and signal-to-noise ratio (abstr). In: Proceedings of the Fifth Meeting of the International Society for Magnetic Resonance in Medicine. Berkeley, Calif: International Society for Magnetic Resonance in Medicine, 1997; 1834.
33. Hilaire L, Wehrli FW, Song HK. High-speed spectroscopic imaging for cancellous bone marrow $R(2)^*$ mapping and lipid quantification. *Magn Reson Imaging* 2000; 18:777-786.
34. Speck O, Hennig J. Functional imaging by $I0$ - and $T2^*$ -parameter mapping using multi-image EPI. *Magn Reson Med* 1998; 40:243-248.

Original Research

Structure of the Water Resonance in Small Voxels in Rat Brain Detected With High Spectral and Spatial Resolution MRI

Xiaobing Fan, PhD, Weiliang Du, MS, Peter MacEneaney, MD, Marta Zamora, BS, and Gregory Karczmar, PhD*

Purpose: To acquire high spectral and spatial resolution (HISS) MR images of the water resonance in rat brain, evaluate the lineshape of the water resonance in small voxels, and compare images derived from HISS data with conventional images.

Materials and Methods: Spectroscopic images of rat brain were obtained at 4.7 Tesla using phase encoding gradients only. Spectral resolution in each voxel was ~ 8 Hz and bandwidth was 1000 Hz. Spatial resolution was ~ 250 microns in 1-mm slices. Images were synthesized to show the water signal integral, peak height, linewidth, resonance frequency, and asymmetry.

Results: Two or more resolved components of the water resonance were detected in $\sim 14\% \pm 6\%$ of voxels in the brains of eight rats. The water resonances in $\sim 20\% \pm 10\%$ of voxels ($n = 8$) were highly asymmetric. Images with intensity proportional to water signal peak height, T_2^* , or to selected components of the water resonance showed features that were not evident in conventional images.

Conclusions: The complexity of the water signal reflects the anatomy and physiology of the sub-voxelar environment, and may be a useful source of image contrast. HISS imaging of brain provides accurate anatomic information, and may improve image contrast and delineation of subtle anatomic features.

Key Words: neuro-imaging; brain imaging; spectroscopic imaging; image contrast; water resonance

J. Magn. Reson. Imaging 2002;16:547-552.

© 2002 Wiley-Liss, Inc.

BRAIN IS AN OPTIMAL TARGET for MRI in part because the water resonance in brain is relatively narrow and

Lorentzian. This is also an advantage for functional imaging studies where very small changes in water signal linewidth must be detected (1,2). However, there is both theoretical (3,4) and experimental (5-7) evidence that the water resonance in small image voxels in brain is inhomogeneously broadened. An important source of spectral heterogeneity is deoxyhemoglobin, which produces microscopic magnetic susceptibility gradients around veins, venules, and capillaries. This is demonstrated by a number of elegant theoretical studies that have modeled BOLD (blood oxygen level dependent) contrast and changes in BOLD contrast during stimulus (e.g., 3,4). Experimental work in this laboratory has shown (8) that different Fourier components of water resonances in small voxels respond differently to changes in tumor oxygenation. Reichenbach et al took advantage of magnetic susceptibility differences between large veins and surrounding tissue to produce "MR venograms" using one and two point spectroscopic imaging (9). Other sources of anatomic heterogeneity, i.e., gray matter vs. white matter vs. CSF (cerebrospinal fluid) may produce more subtle variations in magnetic susceptibility (10-12).

Despite the importance of MRI for clinical neurology and neuroscience, and the dependence of MR images on the structure of the water spectrum, there is little information concerning the water signal in brain. This paper reports a preliminary study using high spectral and spatial resolution to characterize the water signal in very small voxels. Pure absorbance spectra were calculated to improve the effective spectral resolution. The results demonstrate that water resonances in many small voxels in rat brain are complex with two or more resolvable components. Images synthesized from high spectral and spatial resolution (HISS) datasets suggest that information inherent in spectral lineshapes provides novel contrast and anatomic detail in MR images (11,13-16).

MATERIALS AND METHODS

Experimental Protocol

The experimental protocol was approved by the University of Chicago Animal Care and Use Committee (Protocol #53001). The brains of adult Copenhagen and

Department of Radiology, University of Chicago, Chicago, Illinois.

Contract grant sponsor: NCI; Contract grant numbers: 1R01CA76476, 1R01CA78803; Contract grant sponsor: Army Breast Cancer Research Program; Contract grant number: BC981147; Contract grant sponsor: GE Medical Systems.

*Address reprint requests to: G.K., Associate Professor, Department of Radiology, MC2026, University of Chicago, 5841 S. Maryland Ave., Chicago, IL 60637.

E-mail: gskarczm@midway.uchicago.edu

Department of Radiology, University of Chicago, Chicago, IL 60637.

Received February 1, 2002; Accepted June 5, 2002.

DOI 10.1002/jmri.10193

Published online in Wiley InterScience (www.interscience.wiley.com).

Fisher rats weighing 175–210 g were imaged at 4.7 Tesla using a GE/Bruker Omega (Fremont, CA) scanner equipped with self-shielded gradient coils. During the scans, rats were anesthetized by continuous I.P. ketamine (5 mg/100 g per hour) and rompun (0.1 mg/100 g per hour). Body temperature was maintained at 37°C using a warm water blanket and warm air.

An 8-element birdcage coil (4.0 cm in diameter and 4.0 cm long) was used for signal excitation and detection. The rat head was secured with tape in the center of the coil. Localized shimming was performed on a 5-mm slice including the 1-mm slice that was later imaged. Optimal shimming is important (17) in HISS imaging so that spectral details that reflect local anatomy and physiology are not obscured by broadening. To minimize the effects of eddy currents on water signal lineshape, and improve separation of spectral and spatial information (13,15), high resolution spectroscopic images were acquired using phase encoding only, with detection of the proton FID (free induction decay) in the absence of applied gradients (18,19). SI (spectroscopic image) data were acquired using a 128² data matrix, 1-mm slice thickness, and 32-mm² field-of-view. The FID was sampled for 128 msec to obtain spectral resolution of 7.8 Hz and spectral bandwidth of 1000 Hz (128 spectral points). Small flip angles (<25°) were used to reduce stimulated echoes. The total acquisition time required for each spectroscopic image was ~40 minutes. Data were processed by three-dimensional Fourier transform without apodization to obtain a high resolution proton spectrum in each voxel. Only the water resonance was used to construct images; minor signals due to lipids were excluded from analysis.

Conventional spin echo (TR: 2000–4000 msec, TE: 10–75 msec) and gradient echo (TR: 400–2000 msec, TE: 10–30 msec) images were acquired with the same spatial resolution as spectroscopic images. The total acquisition time required for each conventional image was ~4 to ~12 minutes.

Calculation of a Frequency Correction to Minimize Truncation Errors

Truncation effects often occur in HISS datasets because the T_2^* of individual components of the proton FID in very small voxels is sometimes long. The truncation effects were minimized by digitally shifting the frequency of the water (or fat) proton resonance in each pixel until the peak frequency of the major component of the water signal coincided with one of the Fourier components of the discrete Fourier transform. At this point, the amplitude of the water peak in the Fourier domain is maximized. This is taken to be the most accurate estimate of peak amplitude. In principle, this procedure works perfectly only if the water signal is a single narrow Lorentzian. However, we find that in the case of the complicated water signals commonly seen in tumors, the digital frequency shifting procedure improves the estimate of the height of the primary water peak in each pixel and significantly reduces truncation artifacts (20).

Calculation of Pure Absorption and Dispersion Spectra for Each Pixel

A zeroth-order phasing algorithm was used to increase sensitivity to spectral lineshapes. If the phase of the acquired spectrum relative to a pure absorption/dispersion is θ , then its real (R) and imaginary (I) components are related to the pure absorption (U) and dispersion (V) modes by the following equations:

$$U = R \cdot \cos(\theta) + I \cdot \sin(\theta), \quad V = -R \cdot \sin(\theta) + I \cdot \cos(\theta). \quad (1)$$

The integral of the pure dispersion signal is zero, i.e.,

$$\sum V = -\sum R \cdot \sin(\theta) + \sum I \cdot \cos(\theta) = 0, \quad (2)$$

where the summation is over all of the points in the spectra. Eq. [2] can be solved for θ , i.e.,

$$\theta = \tan^{-1} \left(\frac{\sum I}{\sum R} \right). \quad (3)$$

Often, this value of θ is not optimal due to noise and complexity of the water resonance. Therefore, the estimate for θ , was further refined by minimizing the expression:

$$\left| \frac{U_{\min}}{U_{\max}} \right| + \left| \frac{V_{\min} + V_{\max}}{U_{\max}} \right|. \quad (4)$$

This holds because the minimum of the absorption mode signal is zero, and the sum of the minimum and maximum of the dispersion mode signal is zero.

Automatic Detection of Resolved Components of the Water Resonance and of Asymmetric Water Peaks

The number of resolved components of the water resonance and the asymmetry of the spectra were measured from magnitude spectra because the frequency and phase correction method (described above) works well only for the primary component of the water resonance. First, all possible peaks were located, i.e., those points in the spectrum where the signal was larger than at the adjacent frequencies. Then, signal amplitude was measured as the difference between the peak intensity and the local minima between these candidate peaks. Candidate peaks were selected as true peaks if the difference between the local maxima and minima was five times larger than the root mean square of the noise and if, in addition, the peaks were at least 20% of the height of the main peak. Images were constructed to show the location of water spectra with multiple peaks.

To determine the asymmetry of magnitude spectra, the two sides of the spectra on either side of the global maximum were compared. The "Similarity" of the two sides was defined as:

$$\text{Similarity } (S_i, S_h) = \sum (S_i \cdot S_h) / \sqrt{\sum S_i^2} \sqrt{\sum S_h^2}. \quad (5)$$

where S_l and S_h are vectors composed of the low field and high field sides of the magnitude water signal, respectively. The two sides were considered significantly different when "Similarity" was less than 0.95.

Synthesis of Images From HiSS Datasets

A large number of images can be synthesized from HiSS datasets, based on details of the water spectrum. The following methods were used to synthesize images discussed here:

- I. Peak height image: the maximum value of the absorption spectrum (U_{\max}).
- II. Integral image: the summation of the absorption spectrum (ΣU).
- III. T_2^* image: An empirical estimate of the T_2^* line width, which does not assume a functional form of the water resonance, was obtained by dividing the integral by the peak height of each resonance ($\Sigma U/U_{\max} \approx 1/T_2^*$).
- IV. Maximum derivative image: the maximum (or negative minimum) of the derivative of the magnitude spectrum (S'_{\max} or $-S'_{\min}$).
- V. Second moment image: the second moment of power spectra (square of magnitude) about the point (frequency) where the first moment is zero. The second moment of a power spectrum is the mean square of its distribution.
- VI. Images of the intensity of a specific component of the water spectrum: This suppresses signal due to the primary component of the water signal, and emphasizes sub-voxelar anatomic features that appear to have characteristic resonance frequencies determined by local anatomic structure and physiology.

To minimize noise, for methods (II) and (III) the summations were performed only in a limited region around the peak resonance frequency. Images were processed using IDL software (Research Systems, Inc., Boulder, CO).

RESULTS

To test effects of shimming and eddy currents in the absence of motion and physiologic variations, a degassed solution of copper sulphate in a plastic container was used as a phantom. Figure 1 shows the phantom images obtained with: (A) a gradient echo (TR/TE = 1000/30 msec), (B) the B_0 map derived from HiSS data, (C) peak height image obtained from HiSS datasets without frequency and phase correction, and (D) peak height image obtained from absorption spectra with frequency shifting. The spectral and spatial resolutions and field view were exactly the same as for the rat brain images. The truncation artifacts—seen as "zebra stripes" in Fig. 1C—were minimized by the frequency shifting technique (Fig. 1D). The water signals are single, narrow Lorentzians in phantoms of uniform composition, and no complex water peaks were detected, even when shimming was deliberately spoiled using high order shims so that resonance frequency varied by ~140 Hz across the sample.

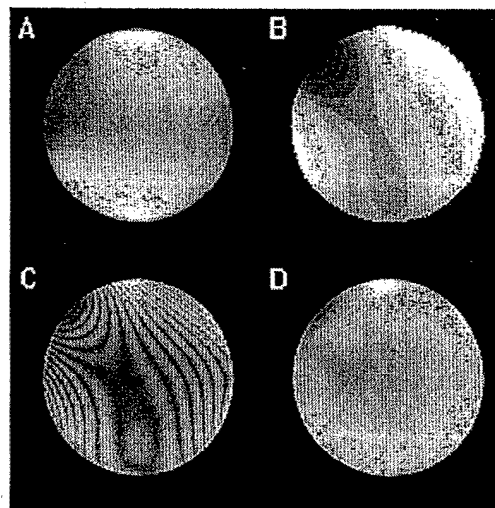


Figure 1. Images of a copper sulphate phantom: (A) Gradient echo image (TR/TE = 1000/30 msec), (B) the B_0 map derived from HiSS data, (C) peak height image obtained from HiSS datasets without frequency and phase correction, and (D) peak height image obtained from absorption spectra with frequency shifting.

The water proton signals in a significant percentage of voxels in rat brain were inhomogeneously broadened and often contained multiple resolvable components. The algorithm described above detected two or more resolved water peaks in an average $\sim 14\% \pm 6\%$ of voxels in the brains of eight rats. Water spectra in an average of $\sim 20\% \pm 10\%$ of voxels ($n = 8$) were asymmetric. Figure 2 shows the distribution of voxels with multiple peaks (column A) or asymmetric peaks (column C) in approximately the same slice in three different rats (column B). The distributions in the three rats are qualitatively similar, and complex water spectra appear to be associated with specific anatomic features. They are most frequently located at well-defined interfaces between different types of tissue, e.g., in tissues adjacent to ventricles where there are dense blood vessels. Examples of water magnitude spectra from two different HiSS datasets are also shown in Figure 2. The spectra in each column are selected from approximately the same location, as indicated by the arrows. Spectra from the same location have similar lineshapes. To test reproducibility, the spectrum from each voxel in one dataset was correlated with the spectrum from the same voxel in a second dataset acquired immediately after the first. The average correlation coefficient obtained in a representative experiment was 0.95 over entire brain.

The complexity of the water signal in many voxels reflects anatomic and physiologic heterogeneity in the local environment, and thus may be a useful source of image contrast. Therefore, we evaluated a number of methods for synthesizing images based on analysis of the water signal lineshape. Figure 3 shows (A) a spin echo image (TR/TE = 3000/50 msec), (B) a T_2^* -weighted gradient echo image (TR/TE = 1000/30 msec), and (C) a T_1 -weighted gradient echo image (TR/TE = 500/10 msec) compared with (D) water signal

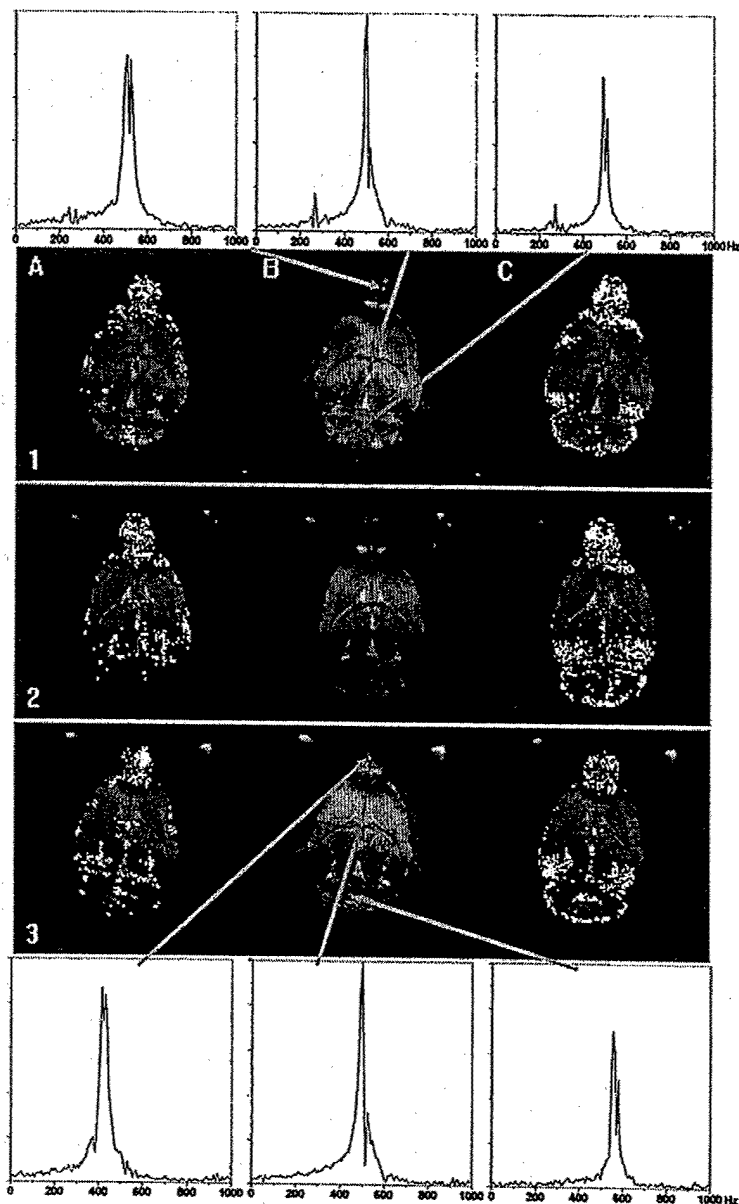


Figure 2. Axial images from approximately corresponding slices in three different rats. Column B shows water resonance peak height images derived from HiSS data. Column A highlights the distribution of pixels with multiple water resonances and column C highlights the distribution of pixels with asymmetric water resonances. Examples of water signal magnitude spectra from two different HiSS datasets are also shown; the locations of the spectra are indicated by the arrows.

peak height, (E) T_2^* , and (F) integral images—all from the same rat brain. The acquisition times required for spin echo and gradient echo images were ~ 12.8 and ~ 6.4 min, respectively, while the acquisition time for the spectroscopic image was ~ 40 minutes. The peak height and T_2^* images synthesized from pure absorption spectra in the HiSS datasets show some features that are not evident in the conventional images. The CSF, cerebellum, hippocampus, caudate putamen, and the central nucleus of the inferior colliculus are particularly clearly defined. The peak height and T_2^* HiSS images in Figures 3D and 3E show dark lines that may correspond to veins, for example, indicated by the arrows. These features are not seen in conventional images.

Further comparisons between conventional images and HiSS images are shown in Figure 4 for three rat brains. Gradient echo T_2^* -weighted images (first column A) are compared with the corresponding peak

height images from HiSS datasets (second column B). In addition, other images obtained from HiSS data using methods IV ("maximum derivative"), V ("second moment"), and VI ("specific frequency component"), as defined in the Methods section, are shown in column C. The gradient echo imaging parameters for rows 1 to 3 were: TR/TRE = 1000/25 msec, 1000/20 msec, and 2000/30 msec, respectively. The corresponding acquisition times were 6.4 minutes, 4.3 minutes, and 12.8 minutes. The peak height images (column B) provide improved contrast, SNR, and enhanced detail, e.g., in the basal ganglion—particularly in row 2, column B, compared to T_2^* -weighted gradient echo images (column A). The maximum derivative image (row 1, column C) shows strong contrast where water spectra have a steeper slope, for example, near the 3rd ventricle indicated by the arrow. The second moment image (row 2, column C) shows features—particularly near the anterior pretectal nucleus indicated by the arrow—that can-

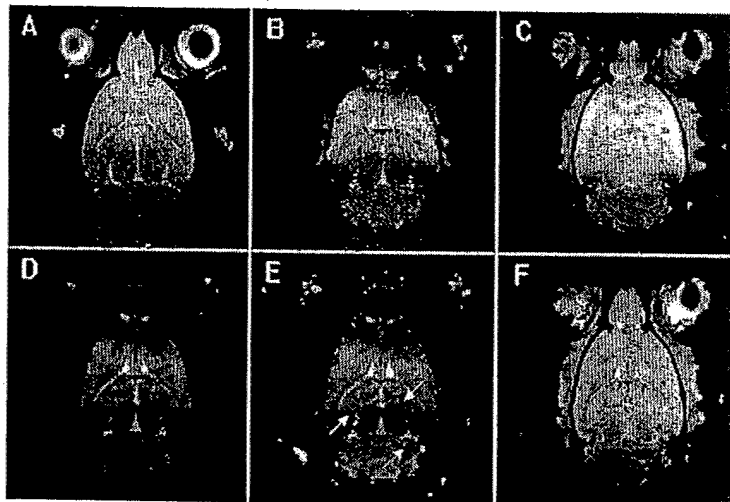


Figure 3. Conventional (A) spin echo, (B) gradient echo T_2^* -weighted, and (C) gradient echo T_1 -weighted images compared with (D) peak height, (E) T_2^* , (F) integral images extracted from the absorption spectra calculated from HiSS datasets.

not be seen in peak height and gradient echo images. Finally, the image from a selected off-peak Fourier component (row 3, column C) shows structures near dentate gyrus and hippocampal area indicated by the arrow that are not seen in gradient echo and peak height images.

DISCUSSION

These results show that many water resonances in small voxels in rat brains are highly non-Lorentzian, with multiple resolved components. The non-Lorentzian spectral features were identified using conservative criteria that probably underestimate the prevalence of complex water spectra in rat brain. The results ob-

tained in phantoms suggest that most of these features are not due to poor shimming or eddy currents. At the spatial and spectral resolution of the present experiments, water resonances from single voxels inside uniform phantoms were single, narrow Lorentzian lines. Poor shimming caused broadening but multiple and asymmetric peaks were not observed. Eddy currents due to phase encoding and slice selection gradients would have been roughly similar in the phantoms and in rat brain, but there were no observable effects of eddy currents in phantoms. This is consistent with the expectation that macroscopic magnetic field gradients, e.g., due to poor shimming or sinuses, are roughly linear across small voxels, and thus will only cause broadening. In fact, the spectral characteristics of water res-

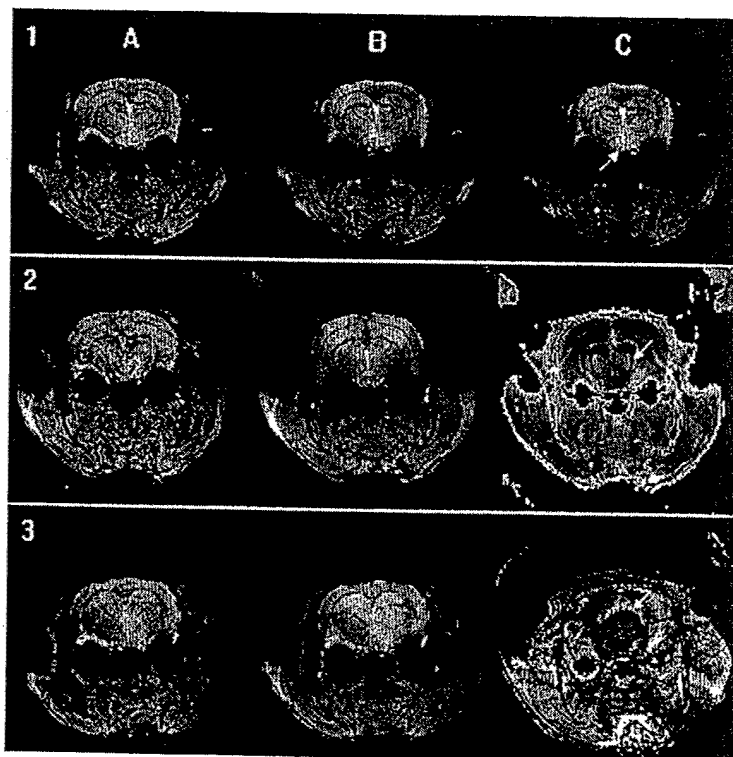


Figure 4. Comparison of gradient echo T_2^* -weighted images (column A) with peak height images (column B) and other images (column C) extracted from the HiSS datasets for three different rats. In column C, rows 1, 2, and 3 are the "maximum derivative", "second moment", and "specific frequency component" images, respectively.

onances in brain appear to be associated with specific anatomic features, rather than with large macroscopic B_0 gradients. This suggests that they are caused primarily by local variations (i.e., subvoxelar or between neighboring voxels) in magnetic susceptibility that reflect the heterogeneity of local anatomy and physiology. For example, small blood vessels or sharp transitions in tissue composition (12) cause shifts in resonance frequency that may produce distinguishable components of the water resonance. Spectral resolution higher than that of the present data (~ 8 Hz) might show more detail than is present in the current images, albeit at the cost of decreased SNR. Ultimately, macroscopic field gradients will limit our ability to detect local gradients in magnetic susceptibility—but this problem can be offset by use of sophisticated shimming methods (21).

This report describes preliminary work. A great deal remains to be done to identify the sources of inhomogeneous broadening in each region, and to determine whether spectral information can be analyzed to produce novel, clinically useful images. Nevertheless, the data suggest potential advantages of high spectral and spatial resolution imaging that merit further examination. HiSS images of normal rat brain show features that are not detectable in conventional images. Sensitivity to specific spectral components may provide information at the sub-voxelar, or perhaps microscopic level (8,15,22).

Qualitative differences between HiSS images and conventional images are probably not due to differences in the signal-to-noise ratio of the images. The acquisition times of HiSS images were substantially longer than for conventional images due to the requirements of the phase encoding method. However, the HiSS datasets were predominantly composed of very low signal components of the proton FID at long evolution times (out to 128 msec), while the T_2^* -weighting of the conventional gradient echo images was much less pronounced (echo times of 10–30 msec). Thus, the overall signal-to-noise ratio of HiSS and conventional images was similar. It is likely that the differences between HiSS and conventional images derive primarily from the fact that the HiSS images are much more heavily T_2^* -weighted than conventional gradient echo images, without the distortions that generally accompany strong T_2^* -weighting, and that blurring due to local susceptibility gradients can be minimized in HiSS images. In addition, HiSS imaging can sometimes distinguish signals from different anatomic structures based on resonance frequency.

Echo planar spectroscopic imaging techniques allow acquisition of HiSS data with dramatically reduced run times and can be used for high resolution anatomic and functional imaging (11,13,14,23) in a clinical setting. Therefore, HiSS MRI of brain can easily be evaluated in patients (2).

ACKNOWLEDGMENTS

GSK thanks Drs. Alan Koretsky, Yiping Du, Charles Springer, and Noam Alperin for their helpful suggestions.

REFERENCES

1. Posse S, Wiese S, Gembris D, et al. Enhancement of BOLD-contrast sensitivity by single-shot multi-echo functional MR imaging. *Magn Reson Med* 1999;42:87–97.
2. Du Y, Du W, Uffring S, et al. fMRI with high spectral and spatial resolution echo-planar spectroscopic imaging at 1.5T. In: *Proceedings of the 9th Annual Meeting of ISMRM*, Glasgow, Scotland, 2001. p 1254.
3. Yablonsky D. Quantitation of intrinsic magnetic susceptibility-related effects in a tissue matrix. Phantom study. *Magn Reson Med* 1998;39:417–428.
4. Ogawa S, Menon RS, Tank DW, et al. Functional brain mapping by blood oxygenation level-dependent contrast magnetic resonance imaging. A comparison of signal characteristics with a biophysical model. *Biophys J* 1993;64:803–812.
5. Menon R, Ogawa S, Tank D, et al. Tesla gradient recalled echo characteristics of photic stimulation-induced signal changes in the human primary visual cortex. *Magn Reson Med* 1993;30:380–386.
6. Zhong J, Kennan R, Schaub M, et al. Measurements of transient contrast enhancement by localized water NMR spectroscopy. *J Magn Reson* 1994;104:111–118.
7. Zhu X, Chen W. Observed BOLD effects on cerebral metabolite resonances in human visual cortex during visual stimulation: a functional (1)H MRS study at 4 T. *Magn Reson Med* 2001;46:841–847.
8. Al-Hallaq HA, Fan X, Zamora M, et al. Spectrally inhomogeneous BOLD contrast changes detected in rodent tumors with high spectral and spatial resolution MRI. *NMR Biomed* 2002;15:28–36.
9. Reichenbach JR, Essig M, Haacke EM, et al. High-resolution venography of the brain using magnetic resonance imaging. *MAGMA* 1998;6:62–69.
10. Ogg RJ, Langston JW, Haacke EM, et al. The correlation between phase shifts in gradient-echo MR images and regional brain iron concentration. *Magn Reson Imaging* 1999;17:1141–1148.
11. Du W, Du Y, Bick U, et al. High spectral and spatial resolution MR imaging of breast. *Radiology* 2002;224:577–585.
12. Peh WC, Chan JH. Artifacts in musculoskeletal magnetic resonance imaging: identification and correction. *Skeletal Radiol* 2001;30:179–191.
13. Kovar DA, Al-Hallaq HA, Zamora MA, et al. Fast spectroscopic imaging of water and fat resonances to improve the quality of MR images. *Acad Radiol* 1998;5:269–275.
14. Sarkar S, Heberlein K, Metzger GJ, et al. Applications of high-resolution echoplanar spectroscopic imaging for structural imaging. *J Magn Reson Imaging* 1999;10:1–7.
15. Karczmar GS, Fan X, Al-Hallaq HA, et al. Uptake of a superparamagnetic contrast agent imaged by MR with high spectral and spatial resolution. *Magn Reson Med* 2000;43:633–639.
16. Zhong K, Li X, Shachar-Hill Y, et al. Magnetic susceptibility shift selected imaging (MESSI) and localized (1)H(2)O spectroscopy in living plant tissues. *NMR Biomed* 2000;13:392–397.
17. Hu J, Javadi T, Arias-Mendoza F, et al. A fast, reliable, automatic shimming procedure using 1H chemical-shift-imaging spectroscopy. *J Magn Reson* 1995;108:213–219.
18. Brown TR, Kincaid BM, Ugurbil K. NMR chemical shift imaging in three dimensions. *Proc Natl Acad Sci U S A* 1982;79:3523–3526.
19. Maudsley AA, Hilal SK, Perman WH, et al. Spatially resolved high resolution spectroscopy by "four-dimensional" NMR. *J Magn Reson* 1983;51:147–152.
20. Fan X, River J, Zamora M, et al. Differentiation of nonmetastatic and metastatic rodent prostate tumors with high spectral and spatial resolution MRI. *Magn Reson Med* 2001;45:1046–1055.
21. Blamire AM, Rothman DL, Nixon T. Dynamic shim updating: a new approach towards optimized whole brain shimming. *Magn Reson Med* 1996;36:159–165.
22. Al-Hallaq HA, Zamora M, Fish BL, et al. MRI measurements correctly predict the relative effects of tumor oxygenating agents on hypoxic fraction in rodent BA1112 tumors. *Int J Radiat Oncol Biol Phys* 2000;47:481–488.
23. Hilaire L, Wehrli FW, Song HK, et al. High-speed spectroscopic imaging at 4T for R2* measurement of individual spectral components. In: *Proceedings of the 7th Annual Meeting of ISMRM*, Philadelphia, 1999. p 257.